

# **A filamentous archaeal virus is enveloped inside the cell and released through pyramidal portals**

Diana Baquero, Anastasia Gazi, Martin Sachse, Junfeng Liu, Christine Schmitt, Maryse Moya-Nilges, Stefan Schouten, David Prangishvili, Mart Krupovic

## **► To cite this version:**

Diana Baquero, Anastasia Gazi, Martin Sachse, Junfeng Liu, Christine Schmitt, et al.. A filamentous archaeal virus is enveloped inside the cell and released through pyramidal portals. Proceedings of the National Academy of Sciences of the United States of America , National Academy of Sciences, 2021, 118 (32), pp.e2105540118. 10.1073/pnas.2105540118 . pasteur-03318874

**HAL Id: pasteur-03318874**

**<https://hal-pasteur.archives-ouvertes.fr/pasteur-03318874>**

Submitted on 11 Aug 2021

**HAL** is a multi-disciplinary open access archive for the deposit and dissemination of scientific research documents, whether they are published or not. The documents may come from teaching and research institutions in France or abroad, or from public or private research centers.

L'archive ouverte pluridisciplinaire **HAL**, est destinée au dépôt et à la diffusion de documents scientifiques de niveau recherche, publiés ou non, émanant des établissements d'enseignement et de recherche français ou étrangers, des laboratoires publics ou privés.

**BIOLOGICAL SCIENCES: Microbiology**

**A filamentous archaeal virus is enveloped inside the cell and released through pyramidal portals**

Short title: Envelopment and release of an archaeal virus

Diana P. Baquero<sup>a,b,#</sup>, Anastasia D. Gazi<sup>c,#</sup>, Martin Sachse<sup>c</sup>, Junfeng Liu<sup>a</sup>, Christine Schmitt<sup>c</sup>, Maryse Moya-Nilges<sup>c</sup>, Stefan Schouten<sup>d,e</sup>, David Prangishvili<sup>a,f,\*</sup> and Mart Krupovic<sup>a,\*</sup>

<sup>1</sup> Archaeal Virology Unit, Department of Microbiology, Institut Pasteur, 75015 Paris, France

<sup>2</sup> Collège Doctoral, Sorbonne Universités, 75005 Paris, France

<sup>3</sup> Unité Technologie et service BioImagerie Ultrastructurale, Institut Pasteur, 75015 Paris, France

<sup>4</sup> Department of Marine Microbiology and Biogeochemistry, NIOZ Royal Netherlands Institute for Sea Research, PO Box 59, 1790AB, Den Burg (Texel), The Netherlands

<sup>5</sup> Department of Geosciences, Faculty of Earth Sciences, Utrecht University, PO Box 80.021, Utrecht, The Netherlands

<sup>6</sup> Faculty of Medicine, Ivane Javakhishvili Tbilisi State University, 0179 Tbilisi, Georgia

# Contributed equally

\* Correspondence to: [david.prangishvili@pasteur.fr](mailto:david.prangishvili@pasteur.fr) and [mart.krupovic@pasteur.fr](mailto:mart.krupovic@pasteur.fr)  
Institut Pasteur, Department of Microbiology,  
75015 Paris, France  
Tel: +33 1 40 61 37 22

**Keywords:** hyperthermophilic archaea, virus egress, Saccharolobus, virus-associated pyramids, virus assembly, archaeal viruses, cell lysis

## ABSTRACT

The majority of viruses infecting hyperthermophilic archaea display unique virion architectures and are evolutionarily unrelated to viruses of bacteria and eukaryotes. The lack of relationships to other known viruses suggests that the mechanisms of virus-host interaction in Archaea are also likely to be distinct. To gain insights into archaeal virus-host interactions, we studied the life cycle of the enveloped, ~2- $\mu$ m-long *Sulfolobus islandicus* filamentous virus (SIFV), a member of the family *Lipothrixviridae* infecting a hyperthermophilic and acidophilic archaeon *Saccharolobus islandicus* LAL14/1. Using dual-axis electron tomography and convolutional neural network analysis, we characterize the life cycle of SIFV and show that the virions, which are nearly two times longer than the host cell diameter, are assembled in the cell cytoplasm, forming twisted virion bundles organized on a nonperfect hexagonal lattice. Remarkably, our results indicate that envelopment of the helical nucleocapsids takes place inside the cell rather than by budding as in the case of most other known enveloped viruses. The mature virions are released from the cell through large (up to 220 nm in diameter), six-sided pyramidal portals, which are built from multiple copies of a single 89-amino-acid-long viral protein gp43. The overexpression of this protein in *Escherichia coli* leads to pyramid formation in the bacterial membrane. Collectively, our results provide insights into the assembly and release of enveloped filamentous viruses and illuminate the evolution of virus-host interactions in Archaea.

## SIGNIFICANCE STATEMENT

Egress of most eukaryotic enveloped viruses, including such human pathogens as HIV-1, Ebola, and coronaviruses, occurs via budding through cellular membranes, a process concomitant with virion assembly. Archaea are also infected by enveloped viruses, but how their virions are assembled and released from the cells remained largely unknown. We show that virions of *Sulfolobus islandicus* filamentous virus (SIFV) are assembled and enveloped in the cell cytoplasm. Instead of budding, SIFV induces the formation of pyramidal structures, which penetrate the cell envelope and serve as portals for virion release. Comparison of the infection cycles of evolutionarily related enveloped and nonenveloped filamentous archaeal viruses suggests that the primary role of the lipothrixvirus membrane is to protect the genome against extreme environmental conditions.

## INTRODUCTION

Hyperthermophilic archaeal viruses are among the most enigmatic members of the virosphere, with many of them displaying unique virion architectures and genomic contents (1-5). The understanding on virus-host interactions in Archaea remains scarce when compared to bacterial or eukaryotic viruses. However, recent studies have provided first insights into different steps of the infection cycle for several model archaeal viruses, showing that some of the mechanisms used by archaeal viruses to interact with the hosts are similar to those of eukaryotic and/or bacterial viruses, whereas others are unique (6-13).

Two major strategies of virion assembly and release have been described for hyperthermophilic archaeal viruses (14). One strategy is exemplified by the *Sulfolobus* spindle-shaped virus 1 (SSV1), the prototypic member of the *Fuselloviridae* family, whereby virion assembly is concomitant with its release via budding through the host cell envelope, closely resembling the release of many eukaryotic enveloped viruses, such as HIV-1 and influenza (7). This release strategy typically does not result in the lysis of the infected cell and, following the eukaryotic virus paradigm, is expected to be common to other enveloped archaeal viruses. By contrast, viruses which assemble virions intracellularly employ egress strategy involving the disruption and death of the host cell. Archaeal viruses have evolved a unique cell lysis mechanism based on the formation of large pyramidal structures, dubbed virus-associated pyramids (VAPs), on the host cell surface (15). The VAPs protrude through the surface protein (S-) layer, the only component of the archaeal cell envelope besides the cytoplasmic membrane (16), and at the end of the infection cycle, the triangular facets of the VAP come apart as flower petals, producing apertures through which the mature virions exit the host cell (6, 17-19). Thus far, the VAP-based egress mechanism has been shown to be used by viruses belonging to three unrelated families, namely, *Rudiviridae*, *Turriviridae* and *Ovaliviridae*, all infecting hyperthermophilic and acidophilic archaea of the order Sulfolobales. The VAPs formed by non-enveloped rod-shaped rudiviruses and icosahedral turriviruses are seven-sided (i.e., the VAP has seven triangular facets) (17, 18, 20) and are built from homologous proteins which, in all likelihood, have been exchanged between viruses from the two families by horizontal gene transfer (21, 22). By contrast, the VAPs built by the ovalivirus SEV1 are six-sided, but the protein responsible for the VAP formation has not been identified (23). Notably, similar six-sided pyramids have been also observed on the surface of hyperthermophilic neutrophiles of the order Thermoproteales (24, 25), suggesting that VAP-based egress strategy is widespread among hyperthermophilic archaeal viruses.

Filamentous viruses of the family *Lipothrixviridae* are among the most broadly distributed archaeal viruses, with representatives being isolated from hot springs in Iceland, Italy, Russia, USA and Japan (24, 26-31). Lipothrixviruses have linear double-stranded (ds) DNA genomes and based on genomic similarities are divided into four genera, *Alphalipothrixvirus*, *Betalipothrixvirus*, *Gammalipothrixvirus* and *Deltalipothrixvirus*. Structural studies have shown that all lipothrixviruses share the same virion organization; namely, linear dsDNA is complexed and condensed by two paralogous major capsid proteins (MCPs) into a helical nucleocapsid, which is further enveloped with a lipid membrane (30, 32, 33). Both ends of the virion are capped with terminal structures responsible for host recognition and binding (10, 27, 28). Similar to several other hyperthermophilic archaeal viruses (34-36), the dsDNA in the nucleocapsid of lipothrixviruses is stored in the A-form (30, 32, 33), which is believed to be one of the adaptations to high temperature environments. Structural studies have shown that lipothrixviruses are evolutionarily related to archaeal viruses of the families *Rudiviridae* and *Tristromaviridae*, but distinct from all other known viruses. Accordingly, the three families have been recently unified into a realm *Adnaviria* (37).

Remarkably, the lipid envelope surrounding the nucleocapsid of lipothrixviruses is twice thinner than the cytoplasmic membrane of the host cell. It has been shown that gammalipothrixvirus AFV1 selectively recruits from the host those tetraether lipid species, which can be bent into a U-shaped horseshoe conformation, and molecular dynamics simulation has further suggested that these lipids form a thin monolayer membrane around the nucleocapsid (32). By contrast, the envelope of alphalipothrixvirus SFV1 is strongly enriched in archaeol, a short lipid molecule corresponding to ~1% of lipids in the host membrane (30). However, whether the viral envelope is acquired during the budding

process, as in the case of the majority of other enveloped viruses (38), remains unknown. Notably, previous studies have suggested that lipothrixviruses are released without causing host cell lysis (26-28), which would be consistent with the budding process, but the exact mechanism has not been investigated.

Here, we characterize the assembly and release of *Sulfolobus islandicus* filamentous virus (SIFV), the type member of the *Betalipothrixvirus* genus. The SIFV virions are enveloped, flexible, filamentous particles measuring ~2  $\mu\text{m}$  in length and 24 nm in width (Figure 1A). At each end of the filament, the SIFV virions are decorated with terminal mop-like structures which are thought to play a role in host recognition (26-28). Using dual-axis electron tomography, we show that the ~2  $\mu\text{m}$ -long SIFV virions are assembled in the cytoplasm of the infected cells which have the diameter of 1-1.2  $\mu\text{m}$ , and are released at the end of the infection cycle through six-sided VAPs. The 89 aa-long SIFV protein gp43 is sufficient for VAP formation and its heterologous overexpression in *Escherichia coli* leads to formation of similar structures in the bacterial membrane. The VAP protein is conserved in all members of the *Betalipothrixvirus* and *Deltalipothrixvirus* genera, but is unrelated to any of the previously characterized VAP proteins from other viruses. Unexpectedly, our results show that, differently from other characterized enveloped viruses, SIFV nucleocapsids are enveloped with a lipid membrane inside the host cell.

## RESULTS

### SIFV infection cycle

To obtain insights into the life cycle of liprothixviruses, we focused on SIFV (26) and its host *Saccharolobus* (formerly *Sulfolobus*) *islandicus* LAL14/1 (39). The *S. islandicus* LAL14/1 cells display an irregular coccoid morphology typical of *Saccharolobus* species with a diameter of  $\sim 1 \mu\text{m}$  (40). Thus, SIFV virions are twice as long as the diameter of the host cell (Figure 1B), indicating that strategies to overcome intracellular space limitation should be in place for efficient virion morphogenesis. We first determined the length of the infection cycle by performing a one-step growth experiment using a multiplicity of infection (MOI) of 0.01. A sharp increase in the extracellular virus titer at 11 hours post infection (hpi), signified the length of the latent period (Figure 1C). With  $26 \pm 7$  virions produced per cell, the burst size is comparable to that determined for the filamentous non-enveloped rudivirus SIRV2 (6). The adsorption assay showed that SIFV binding to the host cells is highly efficient, with nearly 70% of the virions being attached to the host cells within the first 2 minutes post-infection (Figure 1C), ensuring nearly synchronous infection of the *S. islandicus* population. The adsorption rate constant calculated at 2 minutes post-infection was  $5.8 \times 10^{-9} \text{ ml min}^{-1}$ , which is similar to those reported for the turrivirus STIV, rudivirus SIRV2 and bicaudavirus SMV1 (8, 9, 12).

Infection of *S. islandicus* cells using an MOI as low as 0.01 resulted in growth retardation of the culture (Figure 1D), whereas at MOIs  $> 1$  there was a significant decrease in the number of colony forming units (Figure 1E). The effects were more pronounced upon infection with higher MOIs, suggesting that SIFV infection leads to cell death in an MOI-dependent manner. The impact of SIFV on the growth dynamics and viability of the infected cells is reminiscent of those reported for the rod-shaped lytic virus SIRV2 (6), which is structurally and evolutionarily related to SIFV, but is not enveloped (33, 36). Notably, SIRV2 causes massive degradation of the host chromosome upon infection (6). To determine whether this is also the case during SIFV infection, the intracellular DNA content of non-infected and SIFV-infected cultures was monitored over time by flow cytometry. Unlike for SIRV2, there was no host DNA degradation in the case of SIFV-infected cells (Figure S1). Instead, we noted that upon SIFV infection the fraction of cells with a single chromosome copy, especially, after 6 hpi, was diminished. The fact that the majority of infected cells contained two chromosome copies suggests that SIFV infection affects cell cycle control and/or cell division (Figure S1), consistent with the growth retardation of the infected culture (Figure 1D).

### Envelopment of SIFV virions occurs in the host cytoplasm

To gain insights into SIFV virion assembly and envelopment, the infected cells were analyzed using dual-axis electron tomography at 10 and 12 hpi. The reconstructed tomographic volumes were analyzed using convolutional neural networks (CNN) (41) to annotate virions, envelopes, ribosomes and S-layer. At 12 hpi, bundles of filamentous particles resembling SIFV virions were observed (Figure 2A-F), whereas at 10 hpi similar structures were barely detectable (Figure S2A-B). Reconstructed electron tomograms showed that virion-like particles are organized into bundles, which were bent to follow the membrane plane (Figure 2A-C), explaining how the long SIFV virions are spatially accommodated within the host cells. In cross-sections of the infected cells, we could trace up to 70% of the total virion length (i.e.,  $1.4 \mu\text{m}$  out of  $2 \mu\text{m}$ ), with the remaining portion of the virion bundles being invisible, likely due further bending out of the visible plane. Cross-sections showed the presence of  $86 \pm 15$  virions per infected cell ( $n=7$ ), which is about three times higher than the burst size estimated using the plaque test, suggesting that only one third of the assembled virions are infectious (i.e., able to form plaques). The CNN analysis revealed numerous ribosomes, which were distributed evenly in the infected cells (Figure 2), although occasionally, ribosomes were ordered along the viral particles (Figure S3), suggesting either their active role during virion morphogenesis or steric exclusion by the forming virion bundles.

Bundle cross-sections showed that filamentous virions are present in two forms (Figures 2A, 2D, Figure S2B-C): (i) nucleocapsids surrounded by lower density rings that presumably represent the viral envelopes, and (ii) nucleocapsids devoid of any visible envelope (Figure 2D-2F, Figure S2C). Linear density profiles measured across four non-enveloped and enveloped nucleocapsids located adjacent to each other showed that the pixel intensities were the same in the region corresponding to the

nucleocapsid, whereas profiles of enveloped virions had additional intensities at each side of the cross-section profile, representing the viral envelope (Figure 2G-H). Consistent with this interpretation, no significant difference was found between the diameters of the enveloped and non-enveloped nucleocapsid cores (Figure 2I). However, as expected, the center-to-center distances measured between the enveloped nucleocapsids were significantly larger than those between the non-enveloped nucleocapsids, consistent with the additional spacing contributed by the envelopes (Figure 2J).

To further characterize the virion bundles inside the cells, we performed three-dimensional reconstruction of the tomographic data (Figure 3A). Top and lateral views of the 3D models showed that the virion bundles are organized on a non-perfect hexagonal lattice (Figures 3B, 3E) and are slightly twisted (Figure 3B-D). In particular, virions in the periphery of the bundle twist around the virions in the center at 8° angle (Figure 3C-D). Notably, in certain tomograms, the enveloped and non-enveloped virions were parallel to each other and seemingly belonged to the same virion bundle (Figure 2A-C). Collectively, our findings indicate that virion assembly and maturation take place in the cytoplasm of infected cells and proceed through the initial formation of naked nucleocapsids, which undergo sequential envelopment. Intriguingly, this means that envelopment itself occurs in the cytoplasm rather than by extrusion of the naked nucleocapsids through the cellular membrane.

### Characterization of the SIFV envelope

Recent structural characterization of the SIFV virions has revealed that the envelope surrounding the nucleocapsid is twice as thin as the cytoplasmic membrane of the host, as observed for lipothrixviruses from other genera (30, 32, 33). To determine and compare the lipid compositions of the viral and cellular membranes, we performed liquid chromatography with time of flight mass spectrometry (LC-ToFMS) analysis of the mature SIFV virions and *S. islandicus* LAL14/1 cells. The lipid composition of the viral envelope was found to be quantitatively very different from that of the host membrane (Figure 2K). The *S. islandicus* LAL14/1 membrane nearly exclusively contains glycerol dibiphytanyl glycerol tetraether (GDGT) lipid species, long molecules spanning the entire thickness of the membrane, which is effectively a monolayer of GDGT lipids (42). The dominant lipid species (~60% of all lipids) in the host membrane is GDGT-4 carrying four cyclopentane rings (Figure S4). By contrast, the envelope of SIFV is strongly enriched in C<sub>20</sub> sn-2,3-glycerol diphytanyl ether lipid, known as archaeol (Figure S4), and C<sub>40</sub> glycerol trialkyl glycerol tetraether GTGT-0, a tetraether lipid with one C40 biphytanyl and two C20 phytanyl moieties. These two lipid species together account for less than 1% in the host membrane but reach over 40% of lipids in the viral envelope (Figure 2K). Thus, similar to some other archaeal viruses (30, 32, 43, 44), the lipids are incorporated into the SIFV envelope in a highly selective manner, in line with the observation that the envelope is not acquired through the budding process.

### SIFV is released from the cell through hexagonal VAPs

The intracellular envelopment of SIFV virions raises questions regarding the mechanism of their egress from the host cell. Thus, to better understand this last stage of the SIFV life cycle, infected cells were observed by transmission electron microscopy (TEM) at different time points after infection. The TEM analysis at 12 and 24 hpi revealed the presence of 6-sided (hexagonal) apertures on the cell surface (Figure 4A). No such structures were observed on the surface of non-infected cells. Scanning electron microscopy (SEM) confirmed the presence of perforations in the envelope of infected cells at 12 hpi (Figure 4B). The hexagonal apertures closely resemble the opened VAPs previously observed in *Pyrobaculum oguniense* cells (25). Thin section TEM imaging of infected cells revealed the presence of pyramidal structures in SIFV-infected cells (Figure 4C), similar to those previously described for lytic viruses of the families *Rudoviridae*, *Turriviridae* and *Ovaliviridae* (6, 17, 23).

To model the 3D shape of the SIFV-induced VAPs, we used dual-axis electron tomography. The VAPs displayed considerable variation in size: the height (measured from the base to the tip of the VAP) ranged from ~38 to 124 nm and the diameter (measured between the opposite sides of the VAP base) varied from ~48 to 220 nm (*n*=22). The SIFV VAPs grow outwards from the cell membrane, penetrating and disrupting the S-layer of the host cell (Figures 5A and S5). At 12 hpi, when the virions are being released, open VAPs were also detected; VAP opening leads to the loss of intracellular content, including the virions, yielding empty “ghost cells” (Figure S5). Occasionally, SIFV VAPs were

associated with dense spherical bodies (Figure 5A), likely representing storage granules (45), which were also observed in the case of SIRV2- and STIV-infected cells (18, 20). The relevance of these structures for VAP formation and/or virus release remains unknown.

Computational re-slicing of the tomographic volume clearly revealed that the VAPs have a hexagonal base (Figure 5B), consistent with the six-sided apertures observed in the cell envelope by negative stain TEM (Figure 4A-B). A 3D model of a SIFV VAP in closed conformation was obtained by manual segmentation (Figure 5C-D). The reconstruction shows that SIFV pyramids are baseless hollow structures consisting of six triangular sides. Given the presence of VAPs of highly variable sizes, including small VAPs located beneath the S-layer, it is likely that VAP formation is nucleated by a hexameric assembly which develops into the six-sided VAP by gradual growth of the triangular facets.

### **SIFV gp43 is sufficient for VAP formation**

SIFV does not encode identifiable homologs of the previously reported VAP proteins P98 and C92 of rudivirus SIRV2 and turrivirus STIV, respectively (21, 22). Given that the VAPs of rudiviruses and turrivirus are seven-sided (18, 20, 21), whereas those of SIFV are six-sided, it is conceivable that the proteins forming the two types of VAPs might be unrelated. Thus, to identify the protein responsible for formation of the SIFV VAPs, the proteins enriched in the membrane fraction of SIFV-infected cells at 12 hpi were analyzed by SDS-PAGE and LC-MS/MS. Five protein bands (B1-B5) appeared or grew in intensity in the membrane fraction of infected cells at 12 hpi, compared to earlier time points post infection or the non-infected control (Figure S6). The upper bands B1 and B2 (with molecular masses of ~20 and ~24 kDa, respectively), also visible in the membrane fraction of infected cells at 10 hpi, were identified as the two major capsid proteins of SIFV. The bands B3 (~15 kDa), B4 (~12 kDa) and B5 (~9 kDa) were detected exclusively in the membrane fraction of infected cells at 12 hpi (Figure S6). Whereas B3 contained no identifiable virus proteins, LC-MS/MS analysis has shown that bands B4 and B5 contain several viral proteins of unknown function, namely, SIFV gp15, gp43, gp20 and gp71 (Table S1).

The four proteins were analyzed for the presence of predicted N-terminal transmembrane domain (TMD), a feature found in other VAP proteins (21, 22). Only gp43 fulfilled this requirement. To investigate if SIFV gp43 is involved in VAP formation, the corresponding gene was cloned and expressed in *Escherichia coli* Rosetta (DE3) pLys. Protein expression was confirmed by western-blot analysis with anti-6×His antibodies (Figure S7). Electron microscopy analysis of thin sections of gp43-expressing cells 4 hours after induction showed the presence of multiple VAP-like structures on the cytoplasmic membrane of the bacterial cells protruding towards the periplasmic space (Figure 5E). The VAPs were always found in the closed conformation, suggesting that the signal triggering the VAP opening is archaea-specific and might require the presence of additional viral factors. Nevertheless, at 4 h post induction, the optical density of induced cell culture was significantly lower compared to the non-induced control, suggesting that the protein expression and VAP formation are toxic to bacteria. Collectively, these results indicate that gp43 is the only essential structural component of VAPs.

The gp43 of SIFV is 89aa-long and is the shortest VAP protein identified to date (Figure S8). To study the distribution of SIFV gp43 homologs, we performed PSI-BLAST searches against the viral non-redundant protein database at NCBI. SIFV gp43 homologs were found to be conserved in all characterized members of the *Betalipothrixvirus* and *Deltalipothrixvirus* genera of the *Lipothrixviridae* family, but have no identifiable homologs in viruses from other families. Thus, SIFV gp43-like proteins form a new family of VAP proteins, distinct from that including other known VAP proteins from rudiviruses and turriviruses (21, 22). The two protein families display similar features, including the N-terminal TMDs and extensive  $\alpha$ -helical content (Figure S8). However, the pattern of amino acid conservation is distinct in the two families, suggesting that the VAPs have evolved in archaea on at least two independent occasions and that these complex structures can be built from proteins with highly different sequences.

## **DISCUSSION**

In this study, we explored the assembly and egress mechanisms of SIFV, a representative of the family *Lipothrixviridae*. Structural studies have shown that lipothrixvirus virions consist of a helical nucleocapsid enveloped with a thin lipid membrane (30, 32, 33). The nucleocapsid of lipothrixviruses is homologous to the helical capsid of non-enveloped viruses of the *Rudiviridae* family (33, 37), indicating that viruses from the two families have evolved from a common ancestor. Based on phylogenomic and structural studies, it has been suggested that this ancestor was an enveloped virus, resembling lipothrixviruses, and that rudiviruses have emerged by shedding the lipid membrane (33). Given that in most viruses, virion envelope plays key roles during different stages of virus-host interaction, such as genome delivery or virion egress, functional comparison between rudiviruses and lipothrixviruses offers a unique opportunity to study the evolution of virus host-interactions.

In many ways, the SIFV infection process resembles that of rudiviruses. The SIFV infection cycle starts with rapid virion adsorption to the host cell surface. The high rate of adsorption, similar to that documented for other hyperthermophilic archaeal viruses (8, 9, 12, 46), is likely to be important for limiting the exposure of the viral particles to extreme environmental conditions. Notably, however, unlike many other hyperthermophilic archaeal viruses which recognize their hosts through pili (12, 47-49), SIFV has been suggested to bind the receptor located directly within the cellular membrane (26). The latent period of SIFV is rather long (~11 h), which is typical of many other archaeal viruses, and might signify the general adaptation of hyperthermophilic archaeal viruses to spending more time within, rather than outside of the cell. The burst size of SIFV is also similar to that of rudivirus SIRV2 (6). Notably, the particle-to-PFU ratio determined for SIFV is 3:1, meaning that only every third virion forms a plaque. A similar particle-to-PFU ratio, 5:1, was determined for fusellovirus SSV1 (43). More generally, particle-to-PFU ratios are virus-specific and, for eukaryotic viruses, vary from 1:1 to more than 1000:1 (50). The discrepancy between the total number and infectious virions may be due to the presence of immature or defective virions, accumulation of detrimental mutations in the viral genome or activity of antiviral defense systems, which abort a substantial fraction of virus infections.

Electron tomography analysis has provided the first insights into the intracellular assembly of the SIFV virions. The formation of SIFV nucleocapsids is highly reminiscent of the assembly of mature rudivirus virions (6, 18). In the case of both viruses, filamentous (nucleo)capsids are assembled in the cell interior forming bundles containing multiple virions. The SIFV virions in the bundles are arranged on a hexagonal lattice, resembling the tendency of many icosahedral virions to form crystalline-like arrays within the cell cytoplasm (51). The three-dimensional reconstruction has shown that the bundles are twisted at an 8° angle. Although the biological relevance of the SIFV bundle twisting is unclear, a similar behavior has been characterized for many biological filaments and artificial materials, such as carbon nanotube ropes and micropatterned filament arrays (52). Interestingly, it has been concluded that the lowest energy state for a bundle of sufficiently flexible and long filaments is achieved when the bundle is twisted (52). Accordingly, twisting of the SIFV bundles might derive from the geometric frustration of the bulk virion packing and surface energy of non-contacting virions at the boundary of the bundle. In addition to twisting, the bundles undergo a pronounced bending to fit within the cell. Indeed, the bundles of ~2 µm-long SIFV virions follow the inner outline of cytoplasmic membrane. Such bending is not observed in the case of rigid SIRV2 virions, which are ~0.9 µm-long and span nearly entire width of the infected cell. It is tempting to speculate that virion rigidity and dimensions of the host cell limit the genome length of rudiviruses.

Whereas the non-enveloped capsids represent mature virions primed for egress in the case of rudiviruses, the SIFV nucleocapsids have to be further enveloped. Most of the studied enveloped viruses, including filamentous Ebola viruses, escape from their host cells by budding (38, 53, 54). Thus, budding is often considered to be the default mechanism of envelope acquisition in enveloped viruses. Indeed, virion morphogenesis and egress of the archaeal lemon-shaped fusellovirus SSV1 are concomitant and occur at the cellular cytoplasmic membrane via a mechanism highly reminiscent of the budding of enveloped eukaryotic viruses (7). Similarly, archaeal pleolipoviruses and bicaudaviruses have been proposed to use budding as an exit mechanism (13, 55). Hence, the finding that SIFV virions are enveloped inside the cell cytoplasm was unexpected. Using electron tomography, we observed both non-enveloped and

enveloped SIFV virions within the same cell and sometimes as part of the same bundle (Figure 2A-C), suggesting an order of events from non-enveloped nucleocapsids, resembling mature rudivirus virions, to mature, enveloped SIFV virions (Figure S9, Video S1).

In eukaryotes, some viruses acquire envelopes inside the cell by budding through organelles, such as endoplasmic reticulum, nuclear envelope or Golgi complex (56-59). However, internal, membrane-bound compartments have never been observed in *Saccharolobus* or any other archaeal cells, rendering the possibility that SIFV virions are enveloped by budding through intracellular membranes highly unlikely. Recently, it has been shown that insect viruses of the *Nudiviridae* family are enveloped by a distinct mechanism inside the cell, involving extensive remodeling of the nuclear membrane (60). However, unlike in the case of SIFV, nucleocapsids of nudiviruses are enveloped simultaneously with the genome packaging. Consequently, the envelopment of SIFV might occur by a novel mechanism, involving either de novo membrane formation or trafficking of lipids from the cytoplasmic membrane to the virion assembly centers – neither mechanism has been demonstrated for other prokaryotic viruses. Additionally, differences in the composition and thickness of the viral and cellular membranes indicate that the incorporation of lipids into the viral membrane occurs in a highly selective manner. Similarly, selective lipid acquisition has been demonstrated for the lytic turrivirus STIV which, unlike lipothrixviruses, has an internal membrane sandwiched between the icosahedral protein capsid and the dsDNA genome (61). The mechanism of the STIV membrane recruitment remains unclear but has been suggested to involve the archaeal ESCRT-based cell division machinery (62). Recently, it has been suggested that ovoid-shaped archaeal virus SEV1 also acquires its envelope intracellularly (23). Thus, the mechanism of membrane remodeling and envelopment employed by lipothrixviruses might be widespread among evolutionarily unrelated archaeal viruses.

Transmission and scanning electron microscopy analyses showed that SIFV induces formation of VAPs on the surface of infected cells, which gradually grow in size (Figure S9, Video S1). A similar mechanism of virion release has been described for archaeal viruses from families *Rudiviridae*, *Turriviridae* and *Ovaliviridae* (6, 17, 23). Among these, SIFV VAPs more closely resemble VAPs formed by ovalivirus SEV1 (23), because VAPs of both viruses are six-sided, rather than seven-sided as observed for rudiviruses and turriviruses (6, 17). Notably, whereas VAP proteins of rudiviruses and turriviruses share relatively high (55.4%) sequence identity (21, 22), gp43 of SIFV has no homologs in ovalivirus SEV1 and appears to be unrelated to the VAP proteins of rudiviruses and turriviruses (Figure S8). The protein responsible for VAP formation during the ovalivirus SEV1 infection remains unknown, but it is likely to represent yet another protein family. Furthermore, gp43 homologs could not be identified in lipothrixviruses of the *Alphalipothrixvirus* and *Gammalipothrixvirus* genera, suggesting that a considerable diversity of protein families capable of VAP formation remains to be discovered in the archaeal virosphere.

Our results show that expression of gp43 in *E. coli* leads to VAP formation in the bacterial membrane. It should be noted that bacterial and archaeal membranes consist of unrelated lipids: whereas bacterial membranes are bilayers containing phospholipids (fatty acids linked to glycerol moieties by ester linkages), the membrane of *S. islandicus* is largely a monolayer of tetraether lipids (long isoprenoid chains capped on both ends by glycerol moieties through ether linkages). Thus, the inherent ability of the two proteins, lacking any recognizable sequence similarity, to form VAPs in both bacterial and archaeal membranes is remarkable. Whether proteins from the two families have diverged from a common ancestor or have originated independently remains unclear. Regardless, the general replication cycle of enveloped lipothrixviruses and rudiviruses appear to be closely similar, involving formation of helical nucleocapsids which are released through VAPs, suggesting that evolutionary transition from a postulated enveloped lipothrixvirus-like ancestor to the non-enveloped rudivirus-like ancestor did not entail any major adaptations in the mechanisms underlying the virus-host interactions. This finding raises the questions regarding the function of the membrane in lipothrixviruses. We hypothesize that the primary role of the lipothrixvirus envelope is protection of the viral genome in hot and acidic environment. Indeed, structural studies have shown that MCP packing in rigid rod-shaped rudiviruses is tighter than in flexible lipothrixviruses (33). Thus, once the ancestral MCP has evolved towards

forming a more robust virus particle, impermeable to harmful extracellular solutes (36), the membrane layer might have become dispensable and was shed.

## **ACKNOWLEDGEMENTS**

This work was supported by l'Agence Nationale de la Recherche (#ANR-17-CE15-0005-01) project ENVIRA and Emergence(s) project MEMREMA from Ville de Paris (to M.K.). D.P.B. was part of the Pasteur – Paris University (PPU) International PhD Program, which has received funding from the European Union's Horizon 2020 research and innovation programme under the Marie Skłodowska-Curie grant agreement No 665807. UTechS Ultrastructural BioImaging is a member facility of France BioImaging (ANR-10-INSB-0004). The authors would like to thank Thibault Chaze and Mariette Matondo (Proteomics Platform, Institut Pasteur) for help with the proteomics and Anhelique Mets (NIOZ) for support with lipid analysis. We are also grateful for the helpful discussions and support provided by Jacomine Krijnse-Locker.

## **Competing Interests**

The authors declare that they have no competing interests.

## MATERIALS AND METHODS

### *Propagation and purification of virus particles*

*Saccharolobus islandicus* LAL14/1 and *S. islandicus* HVE10/4 (63, 64) were grown aerobically at 75°C, pH 3.5 in rich medium containing 0.2% (wt/vol) tryptone, 0.1% (wt/vol) sucrose, 0.1% (wt/vol) yeast extract and mineral salt solution, as described previously (64).

### *Transmission electron microscopy*

For negative-staining TEM analysis, 5 µl of the samples were applied to carbon-coated copper grids, negatively stained with 2% uranyl acetate (w/v) and imaged with the transmission electron microscope FEI Spirit Tecnai Biotwin operated at 120 kV.

### *Lipid analysis*

Lipids were analysed by LC-ToFMS at NIOZ using an Agilent 1290 Infinity II ultra high performance LC coupled to a 6230 Agilent TOF MS as described by Besseling et al (65).

### *Heterologous expression of SIFV gp43*

The SIFV ORF43 was amplified from a pure SIFV stock and cloned into the pUC19 plasmid. The vector contains an isopropyl β-D-1-thiogalactopyranoside-inducible promoter that was used for the expression of the His-tagged protein. *E. coli* Rosetta(DE3)pLys (Novagen, Merck) cells were transformed with the construct, liquid cultures were grown in 2YS medium and induced with 1 mM IPTG at OD<sub>600</sub> of 0.4-0.6 for 4 hours. The non-induced cell culture was used as a control. Thin sections of *E. coli* cells were prepared as described above. The expression of gp43 was detected by estern blot (see SI Methods)

### *Sample preparation for electron tomography*

Cultures at 10 and 12 hours post infection were pelleted by low-speed centrifugation and resuspended in a minimal volume of rich medium. Samples were taken up into cellulose capillary tubes (Engineering Office M. Wohlwend GmbH) as described previously (66), transferred into the 0.2 mm cavity of a type B sample holder filled with hexadecen and frozen with a high-pressure freezing machine (HPM100, Leica). The samples were subsequently freeze-substituted with 1% OsO<sub>4</sub> in acetone according to the following schedule: -90°C for 24 h, 5°C/h for 12 h, -30°C for 12 h, 10°C/h for 3 h, and 0°C for 1 h in a Leica AFS2 (Leica Microsystems). Cells were rinsed at RT within acetone and slowly infiltrated with low viscosity resin (Electron Microscopy Sciences). After heat polymerization, embedded cells were cut into 70-nm thin sections with an Ultracut R microtome (Leica) and collected on Formvar-coated copper grids. Thin sections (70 nm) were poststained with 4% uranyl acetate for 45 min and Reynold's lead citrate staining during 5 min. Samples were imaged with the transmission electron microscope FEI Spirit Tecnai Biotwin operated at 120 kV. For electron tomography, embedded cells were cut into 200-nm thick sections with an Ultracut R microtome (Leica) and collected on Formvar-coated copper grids. Protein A-gold particles of 10 nm were added on both sides of the sections and stained with 4% uranyl acetate (w/v) and Reynold's lead citrate.

### *Dual-axis electron tomography*

Grids were loaded on a dual-axis tomography holder and observed with a TECNAI F20 Transmission Electron Microscope (FEI) operating at 200kV and equipped with a 4k x 4k CCD camera (Ultrascan 4000, Gatan). Micrographs, tilt series and maps, in low and middle magnifications, were acquired using SerialEM (67, 68). After identifying areas of interest on middle magnification maps, the areas were baked using a total dose of 1,500 e<sup>-</sup>/Å<sup>2</sup>. The continuous tilt scheme was used for the automatic acquisition of micrographs every 1° over a ±55° range at higher magnification (usually 29K or 50K). After the acquisition of tilt series in all areas of interest, grid was manually rotated by 90° to acquire the second orthogonal tilt axis series in the same areas of interest.

Initial image shifts of the tilt series were estimated using IMOD's function tiltcorr (69). Alignments were further optimized in IMOD using the tracing of gold fiducials across the tilt series. Three-dimensional reconstructions were calculated in IMOD by weighted back projection using the SIRT-like radial filter to enhance contrast and facilitate subsequent segmentation analysis. The volumes from the two tilt axes were combined to one using fiducials present in IMOD (70).

## REFERENCES

1. Krupovic M, Cvirkaite-Krupovic V, Iranzo J, Prangishvili D, & Koonin EV (2018) Viruses of archaea: Structural, functional, environmental and evolutionary genomics. *Virus Res* 244:181-193.
2. Prangishvili D, *et al.* (2017) The enigmatic archaeal virosphere. *Nat Rev Microbiol* 15(12):724-739.
3. Munson-McGee JH, Snyder JC, & Young MJ (2018) Archaeal viruses from high-temperature environments. *Genes (Basel)* 9(3):128.
4. Dellas N, Snyder JC, Bolduc B, & Young MJ (2014) Archaeal Viruses: Diversity, Replication, and Structure. *Annu Rev Virol* 1(1):399-426.
5. Iranzo J, Koonin EV, Prangishvili D, & Krupovic M (2016) Bipartite network analysis of the archaeal virosphere: Evolutionary connections between viruses and capsidless mobile elements. *J Virol* 90(24):11043-11055.
6. Bize A, *et al.* (2009) A unique virus release mechanism in the Archaea. *Proc Natl Acad Sci U S A* 106(27):11306-11.
7. Quemain ERJ, *et al.* (2016) Eukaryotic-like virus budding in Archaea. *mBio* 7(5):e01439-16.
8. Quemain ER, *et al.* (2013) First insights into the entry process of hyperthermophilic archaeal viruses. *J Virol* 87(24):13379-85.
9. Uldahl KB, *et al.* (2016) Life cycle characterization of Sulfolobus monocaudavirus 1, an extremophilic spindle-shaped virus with extracellular tail development. *J Virol* 90(12):5693-5699.
10. Pina M, *et al.* (2014) Unique genome replication mechanism of the archaeal virus AFV1. *Mol Microbiol* 92(6):1313-25.
11. Martínez-Alvarez L, Bell SD, & Peng X (2016) Multiple consecutive initiation of replication producing novel brush-like intermediates at the termini of linear viral dsDNA genomes with hairpin ends. *Nucleic Acids Res* 44(18):8799-8809.
12. Hartman R, *et al.* (2019) The Molecular Mechanism of Cellular Attachment for an Archaeal Virus. *Structure* 27(11):1634-1646.e3.
13. Liu J, *et al.* (2021) Virus-induced cell gigantism and asymmetric cell division in Archaea. *Proc Natl Acad Sci U S A* 118(15):e2022578118.
14. Baquero DP, *et al.* (2020) Structure and assembly of archaeal viruses. *Adv Virus Res* 108:127-164.
15. Prangishvili D & Quax TE (2011) Exceptional virion release mechanism: one more surprise from archaeal viruses. *Curr Opin Microbiol* 14(3):315-20.
16. Albers SV & Meyer BH (2011) The archaeal cell envelope. *Nat Rev Microbiol* 9(6):414-26.
17. Brumfield SK, *et al.* (2009) Particle assembly and ultrastructural features associated with replication of the lytic archaeal virus sulfolobus turreted icosahedral virus. *J Virol* 83(12):5964-70.
18. Daum B, *et al.* (2014) Self-assembly of the general membrane-remodeling protein PVAP into sevenfold virus-associated pyramids. *Proc Natl Acad Sci U S A* 111(10):3829-34.
19. Quax TE, *et al.* (2011) Simple and elegant design of a virion egress structure in Archaea. *Proc Natl Acad Sci U S A* 108(8):3354-9.
20. Fu CY, *et al.* (2010) In vivo assembly of an archaeal virus studied with whole-cell electron cryotomography. *Structure* 18(12):1579-86.
21. Quax TE, Krupovic M, Lucas S, Forterre P, & Prangishvili D (2010) The Sulfolobus rod-shaped virus 2 encodes a prominent structural component of the unique virion release system in Archaea. *Virology* 404(1):1-4.

- 535 22. Snyder JC, Brumfield SK, Peng N, She Q, & Young MJ (2011) Sulfolobus turreted  
536 icosahedral virus c92 protein responsible for the formation of pyramid-like cellular  
537 lysis structures. *J Virol* 85(13):6287-92.
- 538 23. Wang H, *et al.* (2018) Novel Sulfolobus virus with an exceptional capsid architecture.  
539 *J Virol* 92(5):e01727-17.
- 540 24. Bize A, *et al.* (2008) Viruses in acidic geothermal environments of the Kamchatka  
541 Peninsula. *Res Microbiol* 159(5):358-66.
- 542 25. Rensen E, Krupovic M, & Prangishvili D (2015) Mysterious hexagonal pyramids on  
543 the surface of Pyrobaculum cells. *Biochimie* 118:365-7.
- 544 26. Arnold HP, *et al.* (2000) A novel lipothrixvirus, SIFV, of the extremely thermophilic  
545 crenarchaeon Sulfolobus. *Virology* 267(2):252-66.
- 546 27. Bettstetter M, Peng X, Garrett RA, & Prangishvili D (2003) AFV1, a novel virus  
547 infecting hyperthermophilic archaea of the genus acidianus. *Virology* 315(1):68-79.
- 548 28. Häring M, *et al.* (2005) Structure and genome organization of AFV2, a novel archaeal  
549 lipothrixvirus with unusual terminal and core structures. *J Bacteriol* 187(11):3855-8.
- 550 29. Liu Y, *et al.* (2019) New archaeal viruses discovered by metagenomic analysis of  
551 viral communities in enrichment cultures. *Environ Microbiol* 21(6):2002-2014.
- 552 30. Liu Y, *et al.* (2018) Structural conservation in a membrane-enveloped filamentous  
553 virus infecting a hyperthermophilic acidophile. *Nat Commun* 9(1):3360.
- 554 31. Vestergaard G, *et al.* (2008) Structure of the acidianus filamentous virus 3 and  
555 comparative genomics of related archaeal lipothrixviruses. *J Virol* 82(1):371-81.
- 556 32. Kasson P, *et al.* (2017) Model for a novel membrane envelope in a filamentous  
557 hyperthermophilic virus. *Elife* 6:e26268.
- 558 33. Wang F, *et al.* (2020) Structures of filamentous viruses infecting hyperthermophilic  
559 archaea explain DNA stabilization in extreme environments. *Proc Natl Acad Sci U S*  
560 *A* 117(33):19643-19652.
- 561 34. Wang F, *et al.* (2020) Structure of a filamentous virus uncovers familial ties within  
562 the archaeal virosphere. *Virus Evol* 6(1):veaa023.
- 563 35. Wang F, *et al.* (2019) A packing for A-form DNA in an icosahedral virus. *Proc Natl*  
564 *Acad Sci U S A* 116(45):22591-22597.
- 565 36. DiMaio F, *et al.* (2015) Virology. A virus that infects a hyperthermophile  
566 encapsidates A-form DNA. *Science* 348(6237):914-7.
- 567 37. Krupovic M, *et al.* (2021) *Adnaviria*: a new realm for archaeal filamentous viruses  
568 with linear A-form double-stranded DNA genomes. *J Virol* doi: 10.1128/JVI.00673-  
569 21.
- 570 38. Rheinemann L & Sundquist WI (2020) Virus Budding. *Reference Module in Life*  
571 *Sciences*, (Elsevier).
- 572 39. Jaubert C, *et al.* (2013) Genomics and genetics of Sulfolobus islandicus LAL14/1, a  
573 model hyperthermophilic archaeon. *Open Biol* 3(4):130010.
- 574 40. Albers SV & Siebers B (2014) The family Sulfolobaceae. *The Prokaryotes: Other*  
575 *Major Lineages of Bacteria and The Archaea*, eds Rosenberg E, DeLong EF, Lory S,  
576 Stackebrandt E, & Thompson F (Springer Berlin Heidelberg, Berlin, Heidelberg), pp  
577 323-346.
- 578 41. Chen M, *et al.* (2017) Convolutional neural networks for automated annotation of  
579 cellular cryo-electron tomograms. *Nat Methods* 14(10):983-985.
- 580 42. Villanueva L, Damsté JSS, & Schouten S (2014) A re-evaluation of the archaeal  
581 membrane lipid biosynthetic pathway. *Nat Rev Microbiol* 12(6):438-448.
- 582 43. Quemín ER, *et al.* (2015) Sulfolobus spindle-shaped virus 1 contains glycosylated  
583 capsid proteins, a cellular chromatin protein, and host-derived lipids. *J Virol*  
584 89(22):11681-91.

- 585 44. Bamford DH, *et al.* (2005) Constituents of SH1, a novel lipid-containing virus  
586 infecting the halophilic euryarchaeon *Haloarcula hispanica*. *J Virol* 79(14):9097-107.
- 587 45. Toso DB, Henstra AM, Gunsalus RP, & Zhou ZH (2011) Structural, mass and  
588 elemental analyses of storage granules in methanogenic archaeal cells. *Environ*  
589 *Microbiol* 13(9):2587-99.
- 590 46. Papathanasiou P, *et al.* (2019) Stable maintenance of the rudivirus SIRV3 in a carrier  
591 state in *Sulfolobus islandicus* despite activation of the CRISPR-Cas immune response  
592 by a second virus SMV1. *RNA Biol* 16(4):557-565.
- 593 47. Wang F, *et al.* (2020) The structures of two archaeal type IV pili illuminate  
594 evolutionary relationships. *Nat Commun* 11(1):3424.
- 595 48. Rowland EF, Bautista MA, Zhang C, & Whitaker RJ (2020) Surface resistance to  
596 SSVs and SIRVs in pilin deletions of *Sulfolobus islandicus*. *Mol Microbiol*  
597 113(4):718-727.
- 598 49. Wang F, *et al.* (2019) An extensively glycosylated archaeal pilus survives extreme  
599 conditions. *Nat Microbiol* 4(8):1401-1410.
- 600 50. McCormick W & Mermel LA (2021) The basic reproductive number and particle-to-  
601 plaque ratio: comparison of these two parameters of viral infectivity. *Virol J* 18(1):92.
- 602 51. Duyvesteyn HME, *et al.* (2018) Towards in cellulo virus crystallography. *Sci Rep*  
603 8(1):3771.
- 604 52. Bruss IR & Grason GM (2013) Topological defects, surface geometry and cohesive  
605 energy of twisted filament bundles. *Soft Matter* 9(34):8327-8345.
- 606 53. Votteler J & Sundquist WI (2013) Virus budding and the ESCRT pathway. *Cell Host*  
607 *Microbe* 14(3):232-41.
- 608 54. Noda T, *et al.* (2006) Assembly and budding of Ebolavirus. *PLoS Pathog* 2(9):e99.
- 609 55. Demina TA & Oksanen HM (2020) Pleomorphic archaeal viruses: the family  
610 Pleolipoviridae is expanding by seven new species. *Arch Virol*.
- 611 56. Roingard P, Hourieux C, Blanchard E, Brand D, & Ait-Goughoulte M (2004)  
612 Hepatitis C virus ultrastructure and morphogenesis. *Biol Cell* 96(2):103-8.
- 613 57. Shi X, van Mierlo JT, French A, & Elliott RM (2010) Visualizing the replication  
614 cycle of bunyamwera orthobunyavirus expressing fluorescent protein-tagged Gc  
615 glycoprotein. *J Virol* 84(17):8460-9.
- 616 58. Risco C, Carrascosa JL, & Frey TK (2003) Structural maturation of rubella virus in  
617 the Golgi complex. *Virology* 312(2):261-9.
- 618 59. Read C, Walther P, & von Einem J (2021) Quantitative electron microscopy to study  
619 HCMV morphogenesis. *Methods Mol Biol* 2244:265-289.
- 620 60. Velamoor S, *et al.* (2020) Visualizing nudivirus assembly and egress. *mBio*  
621 11(4):e01333-20.
- 622 61. Maaty WS, *et al.* (2006) Characterization of the archaeal thermophile *Sulfolobus*  
623 turreted icosahedral virus validates an evolutionary link among double-stranded DNA  
624 viruses from all domains of life. *J Virol* 80(15):7625-35.
- 625 62. Snyder JC, Samson RY, Brumfield SK, Bell SD, & Young MJ (2013) Functional  
626 interplay between a virus and the ESCRT machinery in archaea. *Proc Natl Acad Sci U*  
627 *S A* 110(26):10783-7.
- 628 63. Zillig W, *et al.* (1998) Genetic elements in the extremely thermophilic archaeon  
629 *Sulfolobus*. *Extremophiles* 2(3):131-40.
- 630 64. Zillig W, *et al.* (1993) Screening for *Sulfolobales*, their plasmids and their viruses in  
631 Icelandic Solfataras. *Syst Appl Microbiol* 16(4):609-628.
- 632 65. Besseling MA, *et al.* (2020) The absence of intact polar lipid-derived GDGTs in  
633 marine waters dominated by Marine Group II: Implications for lipid biosynthesis in  
634 Archaea. *Sci Rep* 10(1):294.

- 635 66. McDonald K, *et al.* (2010) "Tips and tricks" for high-pressure freezing of model  
636 systems. *Methods Cell Biol* 96:671-93.
- 637 67. Mastronarde DN (2005) Automated electron microscope tomography using robust  
638 prediction of specimen movements. *J Struct Biol* 152(1):36-51.
- 639 68. Schorb M, Haberbosch I, Hagen WJH, Schwab Y, & Mastronarde DN (2019)  
640 Software tools for automated transmission electron microscopy. *Nat Methods*  
641 16(6):471-477.
- 642 69. Mastronarde DN & Held SR (2017) Automated tilt series alignment and tomographic  
643 reconstruction in IMOD. *J Struct Biol* 197(2):102-113.
- 644 70. Mastronarde DN (1997) Dual-axis tomography: An approach with alignment methods  
645 that preserve resolution. *J Struct Biol* 120(3):343-352.
- 646

## FIGURE LEGENDS

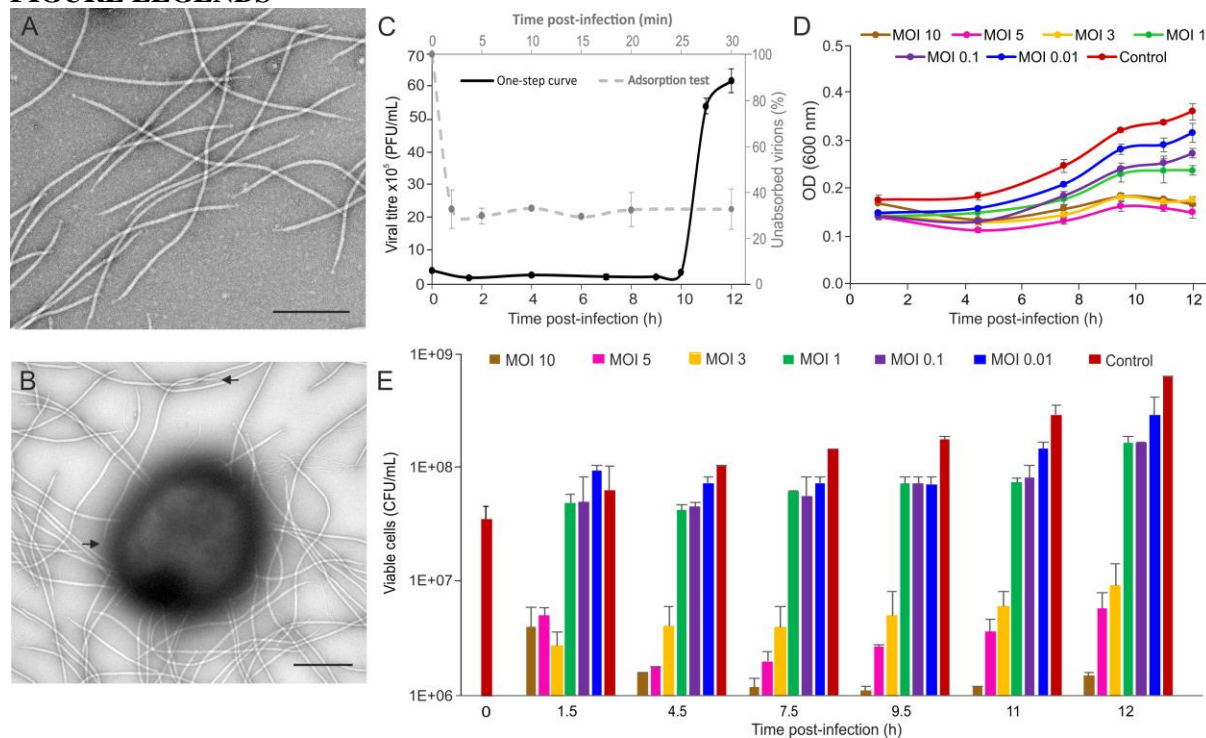


**Figure 1. Characterization of the SIFV infection cycle in *S. islandicus* LAL14/1 cells.** (A) Electron micrograph of purified SIFV particles negatively stained with 2% uranyl acetate. Scale bar, 500 nm. (B) Electron micrograph of *S. islandicus* LAL14/1 cells infected with SIFV. Sample was collected 2 min post-infection and negatively stained with 2% uranyl acetate. Arrows indicate the termini of one selected virion. Scale bar, 500 nm. (C) One-step growth curve (black) and adsorption kinetics (grey) of SIFV using as host *S. islandicus* LAL14/1. For the one-step growth curve and adsorption assay, the cells were infected with an MOI of 0.01 and 0.05, respectively, and the number of extracellular virions was estimated as described in Materials and Methods. (D) Optical density (OD) of *S. islandicus* LAL14/1 liquid cultures infected with SIFV using MOIs ranging from 0.01 to 10. (E) Number of viable cells (CFU/mL) of infected *S. islandicus* LAL14/1 liquid cultures at different MOIs (0.01-10).

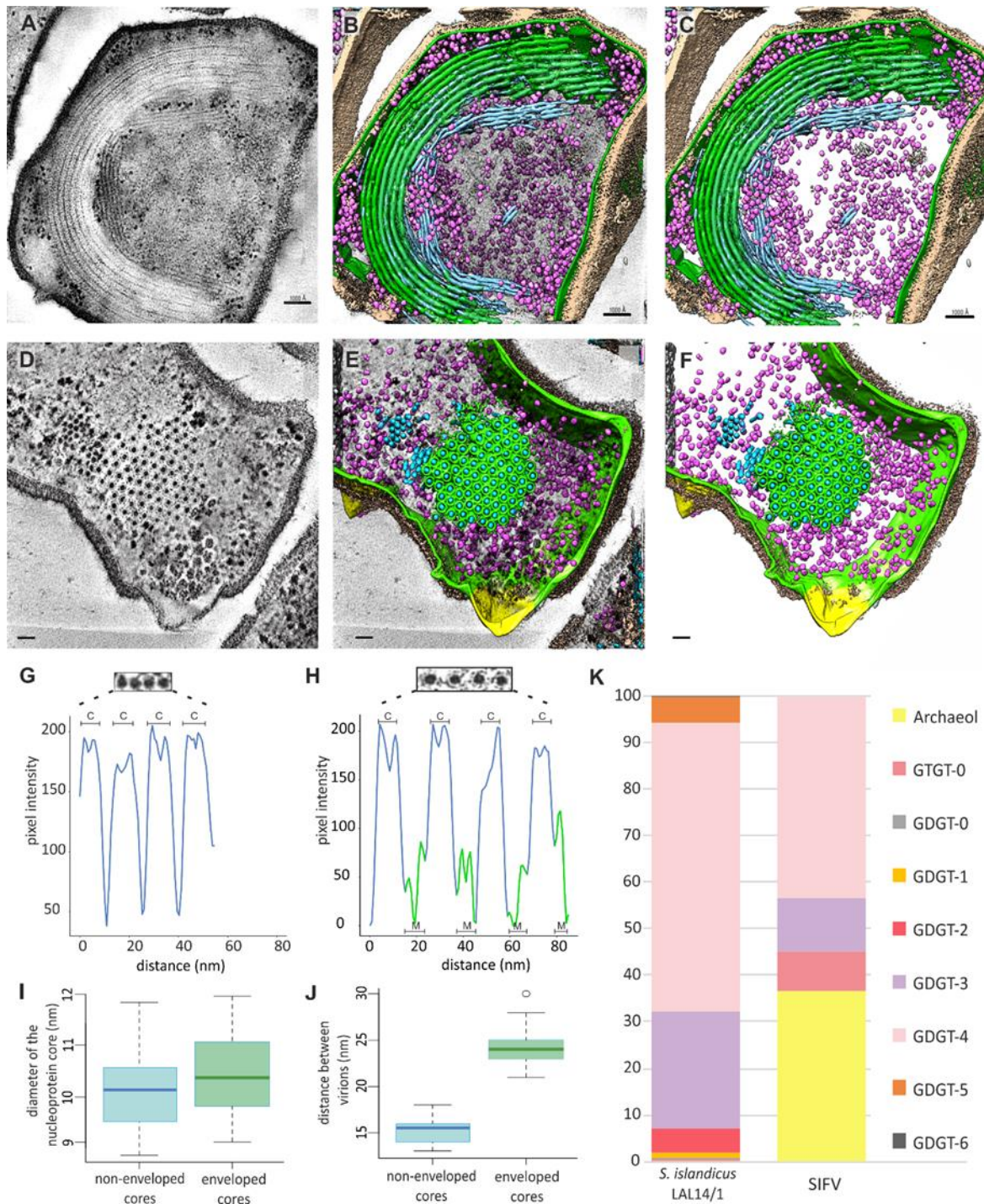


**Figure 2. Assembly of SIFV virions in the cytoplasm of the host cell.** (A) A slice through a reconstructed tomogram of a sectioned sample of SIFV-infected cells at 12 hpi. (B-C) A segmented and surface-rendering displays of the tomogram in panel A, including various viral and cellular components: S-layer (dark salmon), membranes (green), nucleoprotein cores (blue), ribosomes (magenta). (D) A slice through a reconstructed tomogram of a sectioned sample of SIFV-infected cells at 12 hpi, displaying a transversal view of the virions assembled in the host cytoplasm. (E-F) A segmented and surface-rendering displays of the tomogram in panel D: S-layer (dark salmon), pyramid in a closed-conformation (yellow), membranes (green), nucleoprotein cores (blue), ribosomes (light magenta). (G-H) Linear density profiles of four non-enveloped (G) and enveloped (H) nucleocapsids located adjacent to each other. C, nucleoprotein core, M, membrane. (I) Measurement of the diameter (nm) of the nucleoprotein cores of enveloped and non-enveloped virions. (J) Measurement of the distances (nm) between contiguous virions in clusters of enveloped and non-enveloped nucleocapsids. The distance was measured between the centers of adjacent nucleoprotein cores. (K) Distribution of lipid species identified in *S. islandicus* LAL14/1 cells and highly purified SIFV virions. Scale bars, A-C, 100 nm; D-F, 50 nm.

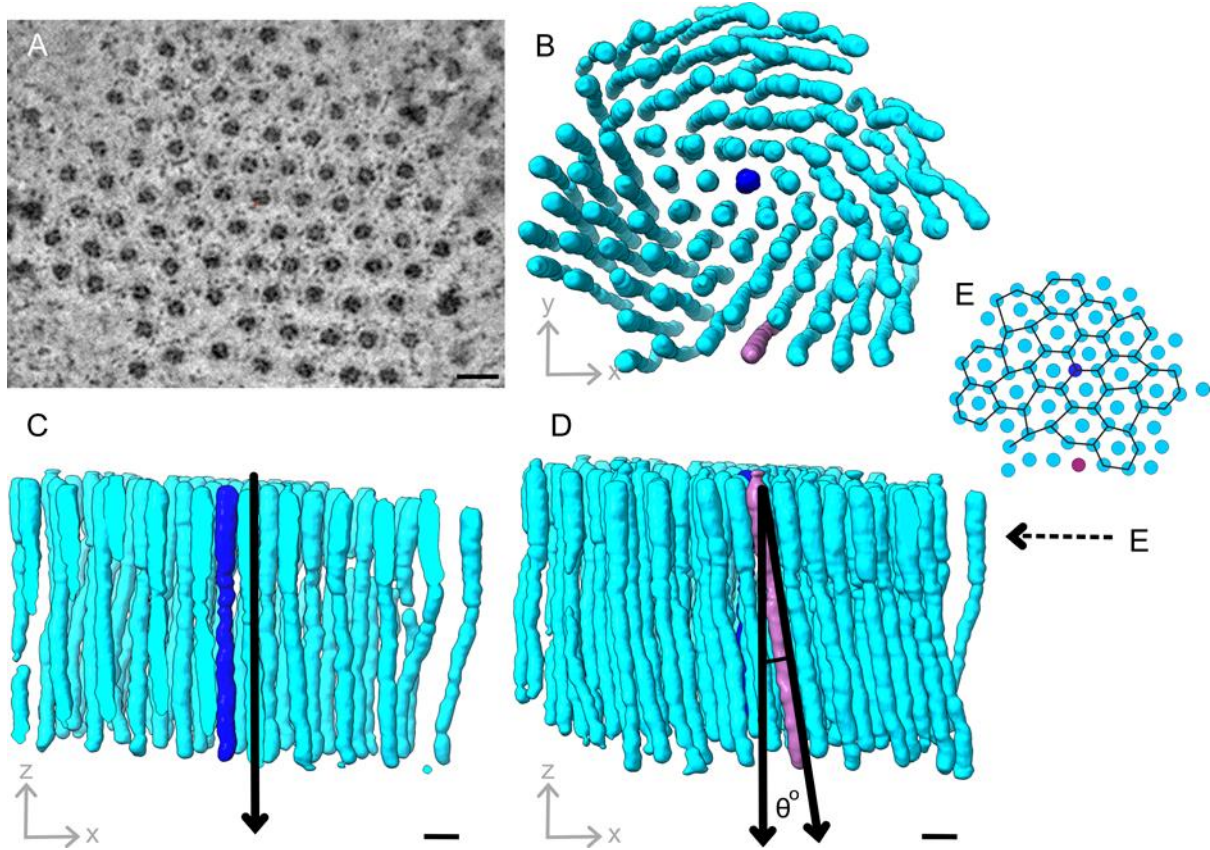


**Figure 3. SIFV virions organized into twisted filament bundles.** (A) A slice through a reconstructed tomogram of a cluster of enveloped virions observed at 12 hpi. (B) Top view of the array of enveloped virions. Virions located at the center (dark blue) and periphery (purple) of the bundle were colored to mark them as positional references. (C) Cross-section through the middle of the array displayed in (B) brought to a vertical orientation. (D) Visualization of the total array displayed in (B). Virions located at the periphery were used to calculate the twist angle  $\theta$  ( $\theta=8^\circ$ ). (E) Black lines trace the non-perfect hexagonal lattice on which the SIFV virions are organized within the bundle shown in panel B.

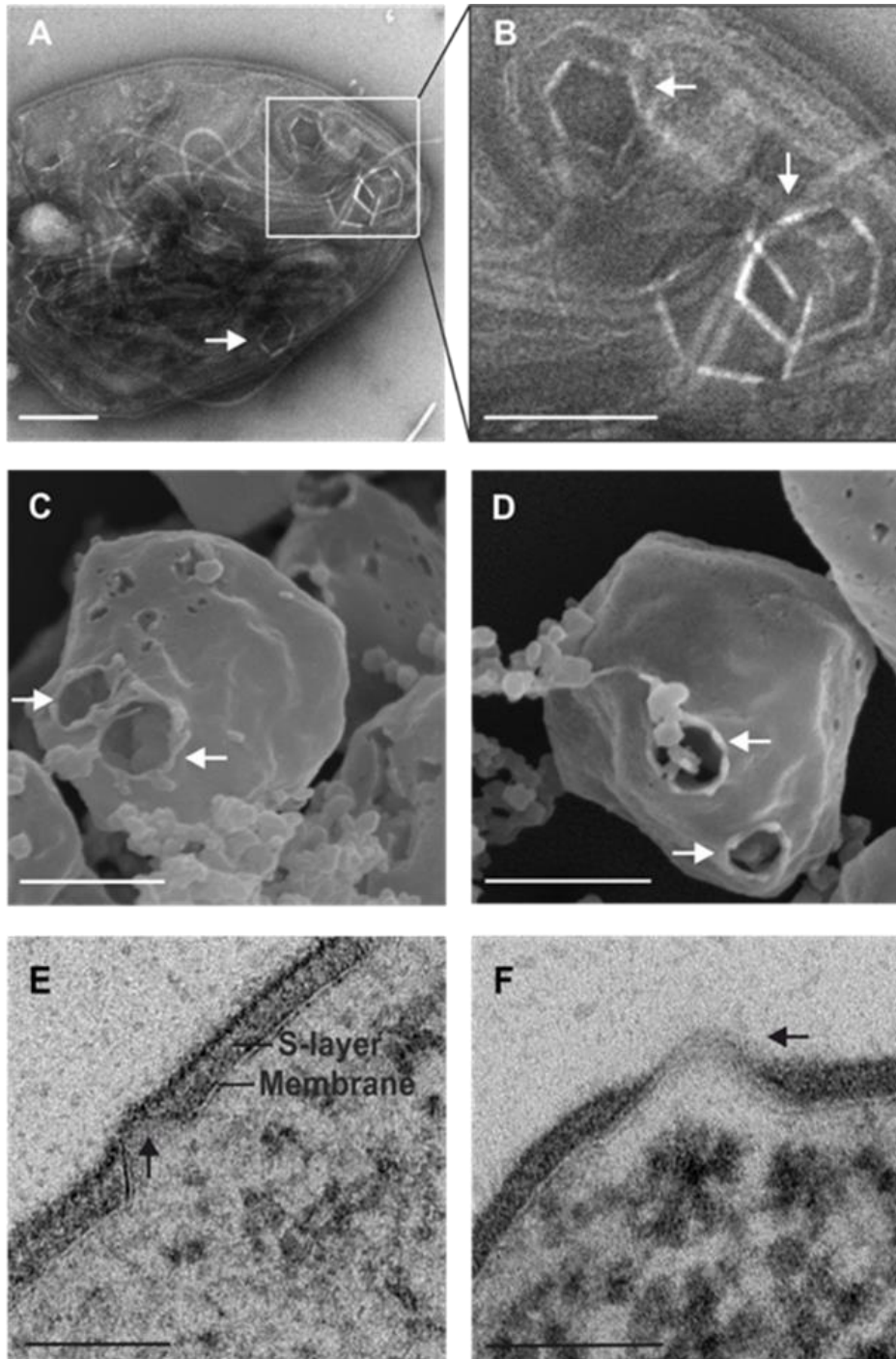


**Figure 4. Visualization of infected *S. islandicus* LAL14/1 cells by TEM and SEM.** (A-B) Infected *S. islandicus* LAL/14 cells collected at 12 hpi, negatively stained with 2% uranyl acetate and visualized under transmission electron microscopy (TEM). (C-D) Infected *S. islandicus* LAL/14 cells collected at 24 hpi and visualized by scanning electron microscopy (SEM). (E-F) Thin sections (70 nm) of infected *S. islandicus* LAL/14 cells collected at 10 hpi and visualized by TEM. Arrows indicate VAPs at different stages. Scale bars: A, 200 nm; B, 100 nm; C, 200 nm; D, 200 nm; E, 200 nm; F, 100 nm.

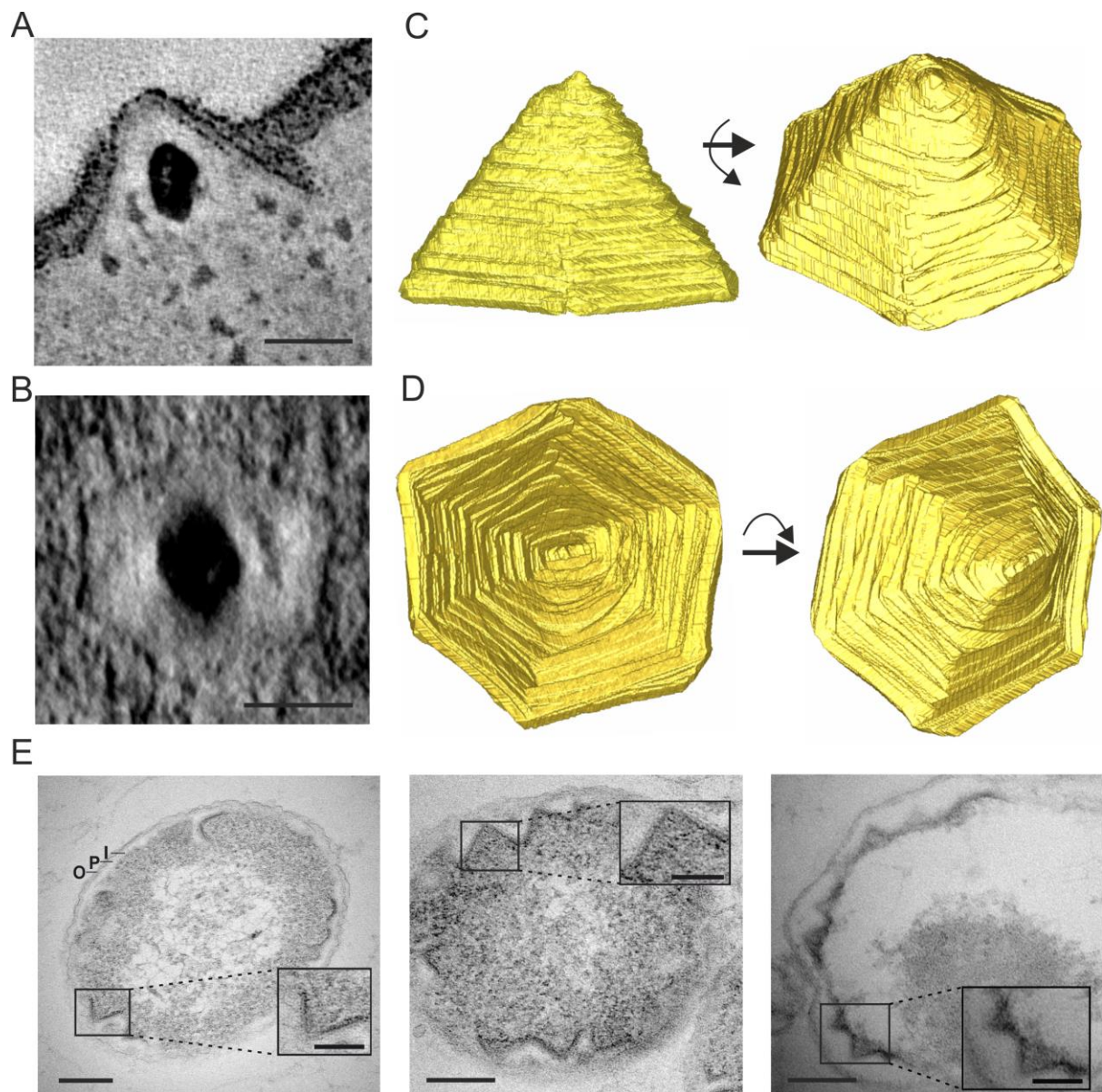


**Figure 5. Visualization of the pyramidal structures formed in the SIFV-infected *Saccharolobus* cells and *Escherichia coli*.** (A) XY slice through a reconstructed tomogram showing the closed conformation of a SIFV VAP. Scale bar, 50 nm. (B) Computed slice view of the same SIFV VAP, aligned to the pyramidal base reveals its hexagonal shape. Scale bar, 50 nm. (C) Lateral view of a 3D map in solid representation of a SIFV VAP. (D) Bottom view of a 3D map in solid representation of a SIFV VAP. (E) Thin section electron micrographs of *E. coli* cells overexpressing SIFV gp43. I, inner membrane, P, periplasmic space, O, outer membrane. Scale bars, 200 nm; in insets: 100 nm.

## SUPPLEMENTARY INFORMATION

### SI Methods

#### *Purification of SIFV virions*

Exponentially growing cultures of *S. islandicus* HVE10/4 and LAL14/1 were infected with the same SIFV preparation and incubated at 75°C under agitation. After two days, cells were removed by centrifugation (7,000 rpm, 20 min, Sorvall 1500 rotor) and viruses were collected and concentrated by ultracentrifugation (40,000 rpm, 2 h, 10°C, Beckman 126 SW41 rotor). The virus titer was determined by plaque assay for both cultures. Although *S. islandicus* HVE10/4 has been characterized as the only susceptible host of the virus (1), we found that the virus propagates more efficiently in *S. islandicus* LAL14/1 (2), a closely related strain (3), yielding higher titers of infectious SIFV particles (Figure S10). Consequently, *S. islandicus* LAL14/1 was used as the host in all subsequent experiments. Early exponentially growing cultures of *S. islandicus* LAL14/1 were infected with fresh preparations of SIFV and incubated at 75°C under agitation. After two days, the infected cell cultures were transferred into fresh cultures (250 mL) of *S. islandicus* LAL14/1 cells and incubated for 2 days. Cells were removed by centrifugation (7,000 rpm, 20 min, Sorvall 1500 rotor) and viruses were collected and concentrated by ultracentrifugation (40,000 rpm, 2 h, 10°C, Beckman 126 SW41 rotor). The concentrated particles were resuspended in buffer A: 20 mM KH<sub>2</sub>PO<sub>4</sub>, 250 mM NaCl, 2.14 mM MgCl<sub>2</sub>, 0.43 mM Ca(NO<sub>3</sub>)<sub>2</sub>, and <0.001% trace elements of Sulfolobales medium, pH 6 (4), and stocked at 4°C until used. For SDS-PAGE, mass spectrometry and lipid analyses, virus particles were further purified by ultracentrifugation in a CsCl buoyant density gradient (0.45 g·mL<sup>-1</sup>) with a Beckman SW41 rotor at 39,000 rpm for 20 h at 10°C. The opalescent bands were collected with a needle and a syringe and dialyzed against buffer A for 2 hours.

#### *Plaque assay*

Serial dilutions of the viral preparations were mixed with preheated *S. islandicus* LAL14/1 cells. Subsequently, 5 mL of pre-heated rich medium containing 0.3% Phytigel™ (Sigma-Aldrich, USA) were added to the prepared mixtures, vortexed and poured into plates containing 0.1% yeast extract, 0.2% sucrose (w/v) and 0.7% Phytigel™ (Sigma-Aldrich, USA) (1). After three days of incubation at 75°C, visible plaques of 0.5-3 mm appeared on the plates.

#### *Adsorption assay*

Exponentially growing cultures of *S. islandicus* LAL14/1 cells were infected with SIFV at an MOI of 0.05. Infected cells were incubated under agitation for 30 min at 75°C. Samples of 1 mL were taken at defined time intervals, cells were pelleted by centrifugation at 8,000 rpm for 10 min (Eppendorf benchtop centrifuge 5415 R), and supernatants were kept at 4°C. The percentage of unadsorbed virus particles was determined by plaque assay comparing the viral concentration in the supernatants with the virus titer in the control. A cell-free control in which SIFV was incubated at 75°C in the growth medium was performed to ensure that the observed decrease in the virus titer is a result of virus adsorption rather than virion inactivation in the harsh conditions, i.e., high temperatures and acidic pH. The virus titer of the cell-free control did not change over the 30 min of incubation. Experiments were conducted in triplicate. The adsorption rate constant ( $k$ ) was calculated using the following formula, as described previously (5):  $k = 2.3/B_t \times \log_{10}(P_0/P_t)$ , where  $B_t$  = concentration of cells at a specific time  $t$  (cell/mL),  $P_0$  = concentration of the virus at zero time (PFU/mL) and  $P_t$  = concentration of not adsorbed viruses at a specific time  $t$  (PFU/mL).

#### *One-step growth curve*

The virus was added to early exponentially growing cultures of *S. islandicus* LAL14/1 cells at an MOI of 0.01. After 30 min of incubation at 75°C, the cultures were diluted in prewarmed medium to prevent the occurrence of new events of adsorption during the experiment. The diluted cultures were incubated at 75°C under agitation. Samples of 1 mL were collected at defined time points and immediately centrifuged at 8,000 rpm for 10 min (Eppendorf benchtop centrifuge 5415 R), to separate the free viruses (supernatant) from the cells (pellet). The PFU titers at different time points were determined by plaque assay. The burst size was estimated by dividing the average amount of viruses present in the supernatants after virus release (11-12 hpi) by the average amount of viruses present in the supernatants before release (0-10 hpi) (6). Experiments were conducted in triplicate.

#### *Infection studies*

Exponentially growing cultures of *S. islandicus* LAL14/1 were infected with SIFV using an MOI range of 0.01 to 10 and incubated at 75°C with shaking. Samples of 1 mL were collected from each culture at defined time points, and the cell density (OD<sub>600</sub>) and the number of viable cells (CFU) were measured. The CFU counting was carried

out as described previously (6). Non-infected cultures were used as controls. Experiments were conducted in triplicate.

#### *Fractionation of the SIFV-infected and non-infected S. islandicus LAL14/1 cells*

The protein content of SIFV-infected cells was established as described previously with minor modifications (7). Briefly, an exponentially growing culture of *S. islandicus* LAL14/1 was infected with SIFV at a MOI of 3. Liquid samples were collected at determined time points and cells were pelleted using low speed centrifugation. Concentrated cells were resuspended in 20 mM Tris-HCl pH 7 and disrupted by sonication (6 cycles with 20 s of sonication and 40 s of pause) or by passage three times through a French pressure cell at a pressure of 800 psi, with the lysate collected on ice. The method used for cell disruption did not affect the subcellular localization of the viral proteins. Unbroken cells were removed from the total cell lysate by low-speed centrifugation. Membrane and cytosol fractions were separated by high-speed centrifugation at  $100,000 \times g$  for 40 min at 4°C. The membrane fraction was resuspended in 20 mM Tris-HCl pH 7. The proteins in each fraction were solubilized in 1% n-Dodecyl  $\beta$ -d-maltoside and incubated at 1 hour at 37°C. Samples were heat-denatured in the presence of SDS sample loading buffer and 1.25%  $\beta$ -mercaptoethanol. Proteins were separated by electrophoresis on a precast NuPAGE gel 4-12% Bis-Tris Bolt (ThermoFisher) and visualized with Instant Blue™ staining (Expedeon).

#### *Mass spectrometry*

The stained protein bands were excised from the gel and in-gel digested with trypsin. The generated peptides were separated and identified by nano-LC-MS/MS (Proteomics Platform, Institut Pasteur) using an Ultimate 3000 system (Dionex) coupled to an LTQ-Orbitrap Velos system (Thermo Fisher Scientific). Peptide masses were searched against annotated SIFV and *S. islandicus* LAL14/1 proteomes using Andromeda with MaxQuant software, version 1.3.0.5.

#### *Western blot*

Induced and non-induced *E. coli* cells were harvested by centrifugation at low speed and resuspended in 20 mM Tris-HCl pH 7. Samples were heat-denatured in presence of SDS sample loading buffer and, optionally, 10 mM dithiothreitol (DTT) as reducing agent, and loaded onto a 4-12% polyacrylamide Bis-Tris gradient gel. Proteins were transferred onto a PVDF membrane. The presence of the 6×His-tagged SIFV gp43 was visualized using a 1:10,000 dilution of the rabbit polyclonal Anti-6X His tag® antibody conjugated with HRP (Abcam).

#### *Flow cytometry*

Non-infected and SIFV infected *S. islandicus* LAL14/1 cells were collected at defined time intervals and fixed with 70% cold ethanol overnight. The fixed cells were pelleted by centrifugation at low speed and resuspended in 1 ml of PBS buffer. Cells were pelleted a second time and resuspended in 70  $\mu$ L of staining buffer containing 40  $\mu$ g/ml propidium iodide (PI). After staining (>30 min), the samples were analyzed for DNA content using an ImageStreamX MarkII Quantitative imaging analysis flow cytometry (Merck Millipore, Germany). The data of 100,000 imaged cells or particles were collected from each sample and analyzed for DNA content by IDEAS data analysis software. The experiment was conducted in triplicate.

#### *Preparation of thin sections using chemical fixation*

Samples at determined time points were fixed by adding glutaraldehyde to the growth medium to a final concentration of 1% during 2 h at room temperature. Cells were pelleted down and resuspended in 20  $\mu$ L in 0.1M Hepes, pH 7. The suspensions were mixed with 20  $\mu$ L of low melting point agar (type VII) and solidified on ice. After solidification, the samples were cut into small pieces, post fixed in 1% osmium tetroxide in 0.1M cacodylate for 1 h on ice, dehydrated in graded ethanol series, infiltrated in propylenoxide:Epon (1:1) and final infiltrated in pure Epon. Samples were transferred into embedding molds and polymerized for 48h at 60°C. Embedded cells were cut into 70-nm thin sections with an Ultracut R microtome (Leica) and collected on Formvar-coated copper grids. Thin sections (70 nm) were stained and imaged with the transmission electron microscope FEI Spirit Tecnai Biotwin operated at 120 kV.

#### *Scanning electron microscopy*

Liquid cultures of infected *S. islandicus* LAL14/1 cells were fixed with 2.5% glutaraldehyde for 2 hours at room temperature. Afterwards, fixed cells were washed in 0.1 M HEPES buffer pH 7.2, post fixed for 1 h 30 in 1% osmium tetroxide in 0.1 M HEPES buffer pH 7.2 and rinsed with distilled water. Samples were dehydrated through a graded series of ethanol (25, 50, 75, 95 and 100%), followed by critical point drying with CO<sub>2</sub>. Dried specimens were sputtered with 20 nm gold palladium using a GATAN Ion Beam Coater and examined and photographed

with a JEOL JSM 6700F field emission scanning electron microscope operating at 7 Kv. Images were acquired from the upper SE detector (SEI).

#### *Segmentation and analysis of tomographic data*

Tomograms were displayed and analyzed using the 3dmod interface of IMOD (8). Archaeal cellular membranes were modeled with manual tracing every 40 slices and the use of IMOD's interpolator. Closed or open contours were used, depending if a full archaeon was included in the field of view or not, respectively. Pyramids of interest were manually traced using IMOD's Slicer to orient the planes for tracing parallel to the pyramid's base, so the hexagonal shape was easily identifiable. Traced models were meshed to surfaces using the imodmesh function of IMOD. Meshed models were finally used to calculate density maps from them in eman2 (9). For the rest of the features that were easily identified: S-layer, ribosomes, virion main bodies and envelope of virions; training sets were prepared based on positive and negative segmentation examples in order to train the convolutional neural network (CNN) algorithms implemented in eman2.3 (9). Final segmentation results were visualized as iso-surfaces with UCSF Chimera (10). Many false positives were removed by thresholding out smaller sized particles for each feature using the 'Hide Dust' tool of UCSF Chimera. For the representation of the S-layer, the CNN segmentation result was used as a mask and the S-layer iso-surfaces were produced based on the original density map of the volume data.

## SI Figures

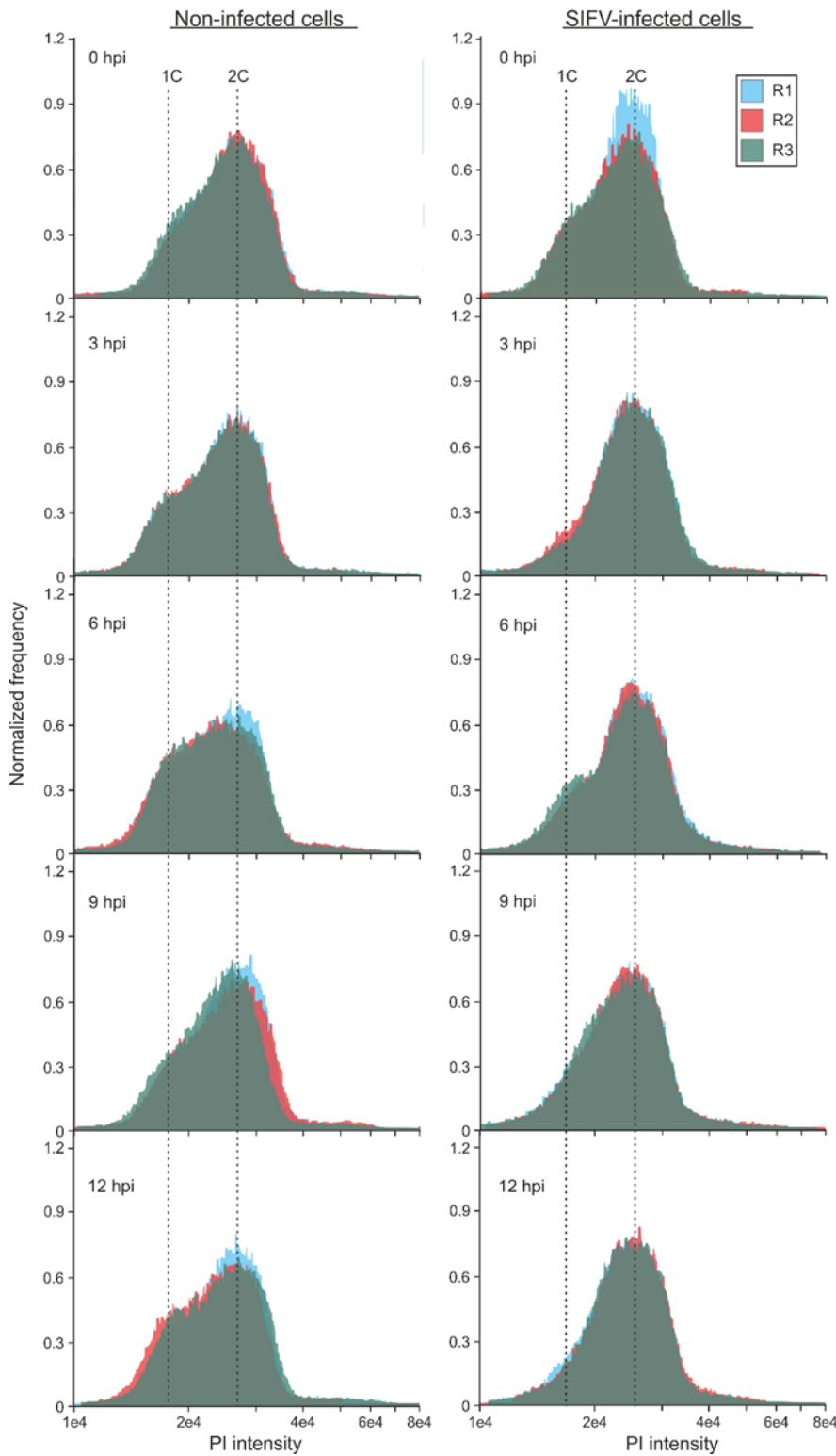


**Figure S1. Flow cytometry analysis of non-infected and SIFV-infected *S. islandicus* LAL14/1 cells.** Cell cultures were sampled and analyzed in triplicates (R1-R3) at the indicated time points. Dotted lines indicate cell populations with the DNA content corresponding to the equivalents of one and two copies (1C and 2C) of genomic DNA. LAL14/1 cells were infected with SIFV using an MOI  $\approx 3$ . The distribution of the DNA content, stained with propidium iodide (PI), was measured as described in Materials and Methods.

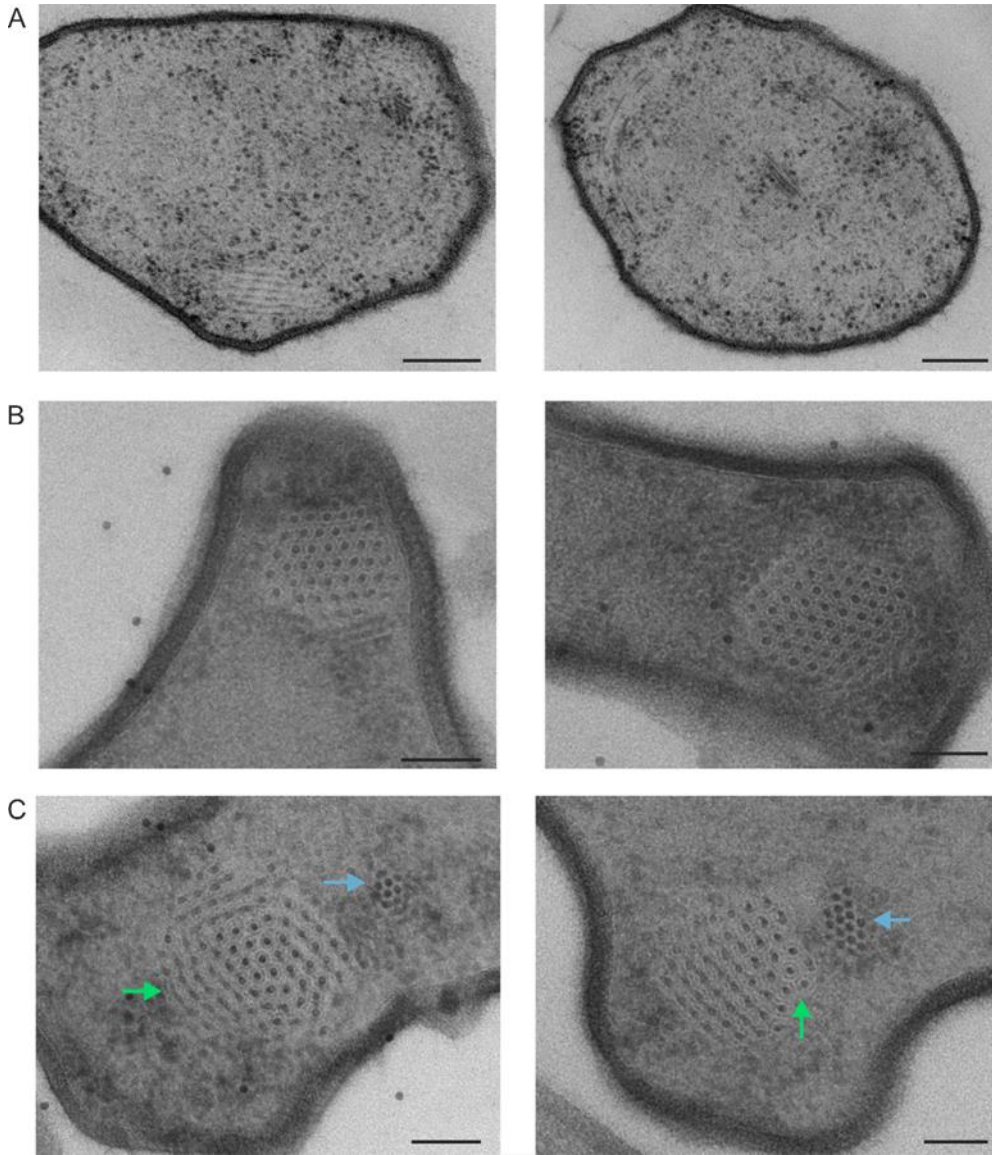


**Figure S2. Slices through reconstructed tomograms of *Saccharolobus islandicus* LAL14/1 infected cells at 10 and 12 hpi.** (A) Slices displaying SIFV infected cells at 10 hpi. (B) Slices displaying SIFV infected cells at 12 hpi. (C) Slices displaying SIFV infected cells at 12 hpi, wherein clusters of enveloped and non-enveloped nucleocapsids are highlighted with green and blue arrows, respectively. Scale bars, 100 nm.

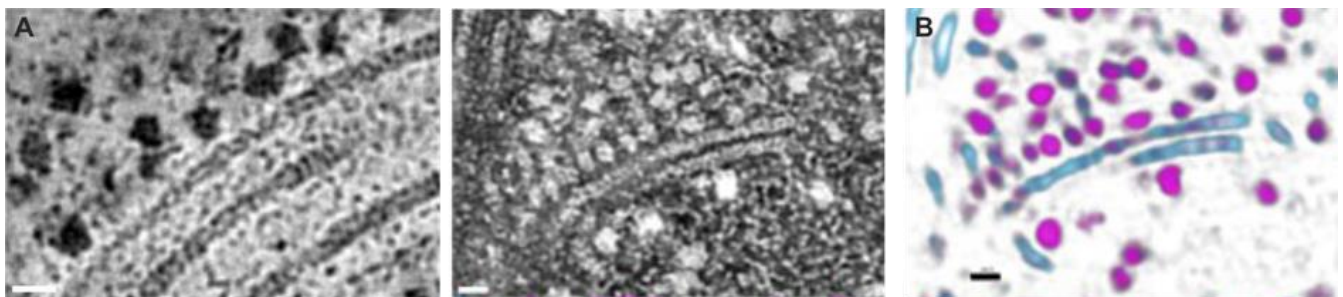


**Figure S3. Visualization of ribosomes-like structures localized around the viral particles.** (A) Slices through reconstructed tomograms displaying ribosomes-like structures ordered along the SIFV virions. (B) Ribosomes (purple) lining along the virion particles (blue) annotated by a convolutional neural network (CNN) algorithm. Scale bar, 20 nm.

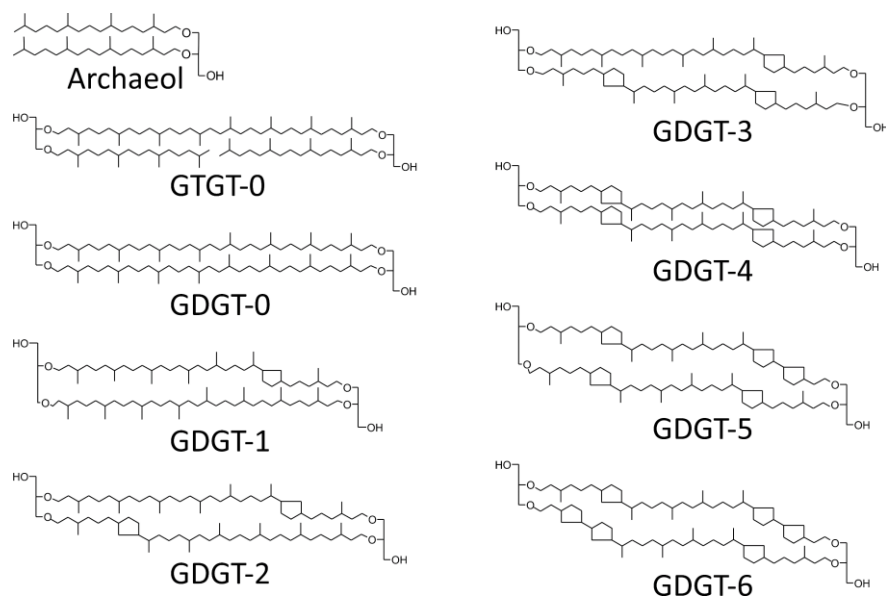


**Figure S4. Chemical structures of the lipid species identified in SIFV virions and *S. islandicus* LAL14/1 cells.**

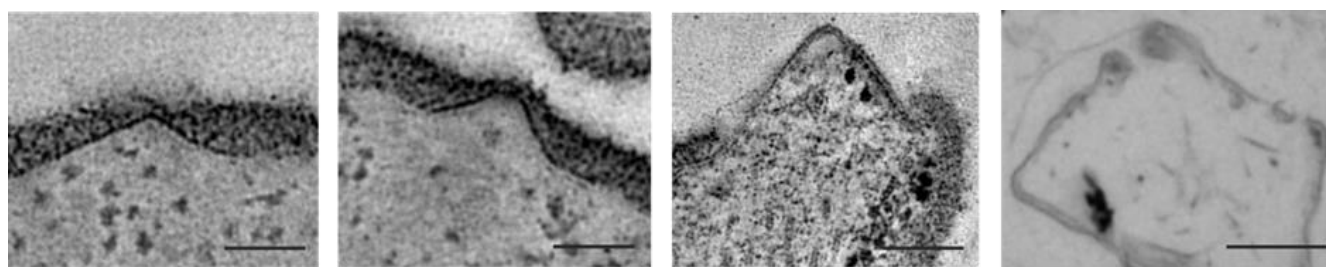


**Figure S5. Visualization of the different stages of SIFV VAPs.** The first three panels correspond to slices through reconstructed tomograms showing SIFV VAPs with variable sizes, whereas the last panel was observed from a thin section electron micrograph displaying a lysed cell upon the aperture of a pyramidal structure. Scale bar, first three panels 100 nm, last panel 400 nm.

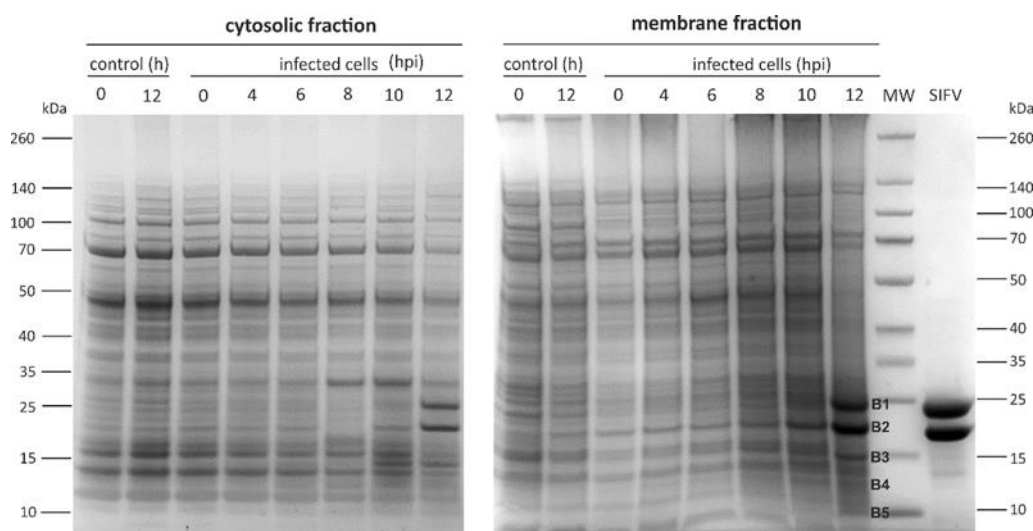


**Figure S6. Identification of the viral protein involved in VAP formation.** Stained SDS-PAGE gels of the cytosolic and membrane fractions of *S. islandicus* LAL14/1 cells infected with SIFV. Cellular fractions were prepared as described in Materials and Methods. B1-B5 labelling denotes the protein bands that appeared in the membrane fraction as a result of the infection. MW, molecular weight marker.

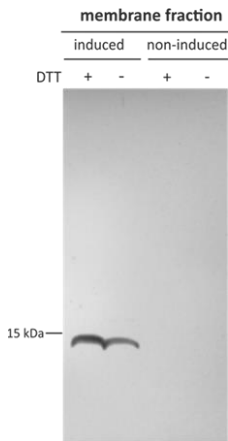


**Figure S7. Detection of the 6×His-tagged SIFV gp43 in induced *E. coli* cells by western blot.** Membrane fractions of induced and non-induced samples were collected at 4 hours post-induction. The effect of DTT on the collected fractions was tested.

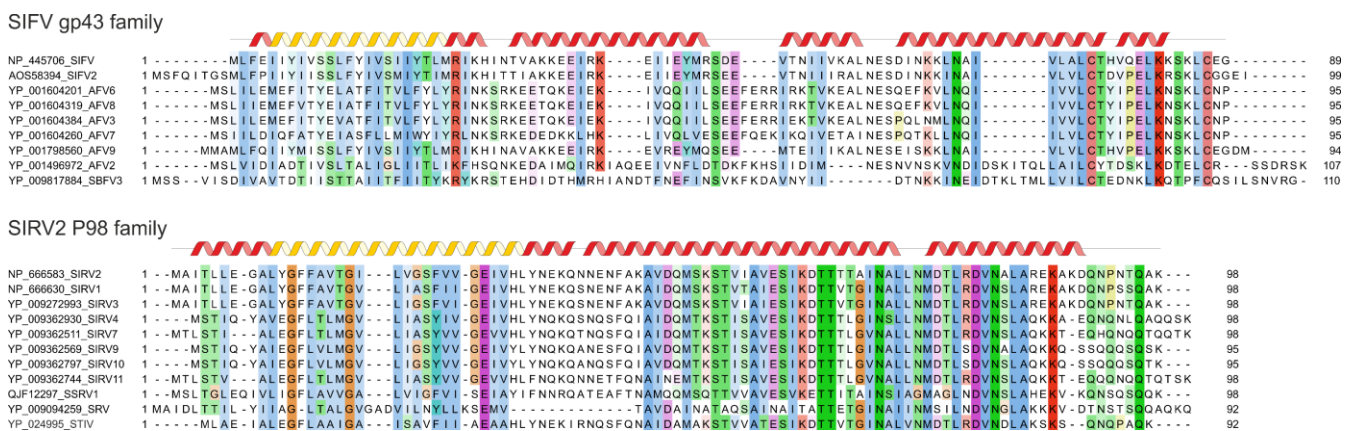


**Figure S8. Multiple sequence alignment of the VAP families represented by SIFV gp43 (top) and SIRV2 P98 (bottom).** Secondary structure was predicted using PSI-Pred and is shown above the corresponding alignments. Predicted  $\alpha$ -helices are shown as ribbons. Yellow ribbons represent the segments predicted to form  $\alpha$ -helical transmembrane domains. Each protein is labelled with the corresponding accession number.

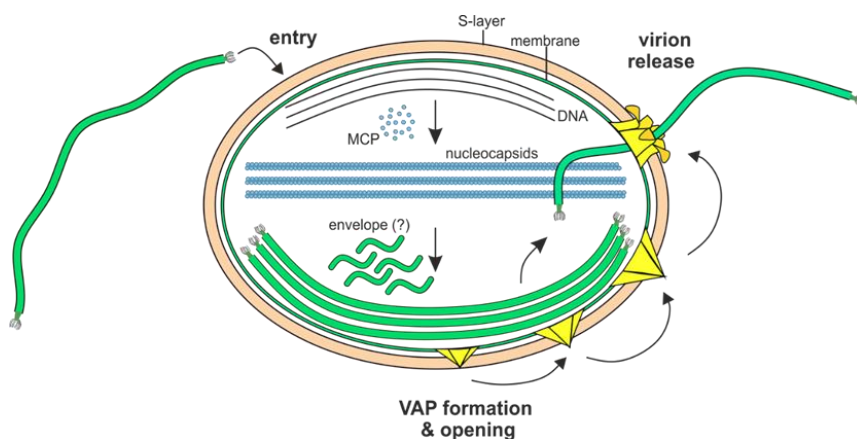


**Figure S9. A schematic representation of the SIFV life cycle.** The infection starts when the virus binds to its specific host receptor; subsequently, the virus delivers its genetic material into the cell through an unknown mechanism. The viral genome is replicated, and nucleoprotein cores are formed in the cytoplasm by binding of heterodimers of the two MCPs to the linear DNA. Concomitantly with the virion assembly, hexagonal virus-associated pyramids (VAPs) start growing on the surface of infected cells. The formation of mature virions is accomplished when the nucleoprotein cores are enveloped in the cytoplasm through an unclear mechanism. Subsequently, the pyramidal structures disrupt the S-layer and open to produce apertures through which the mature virions exit.

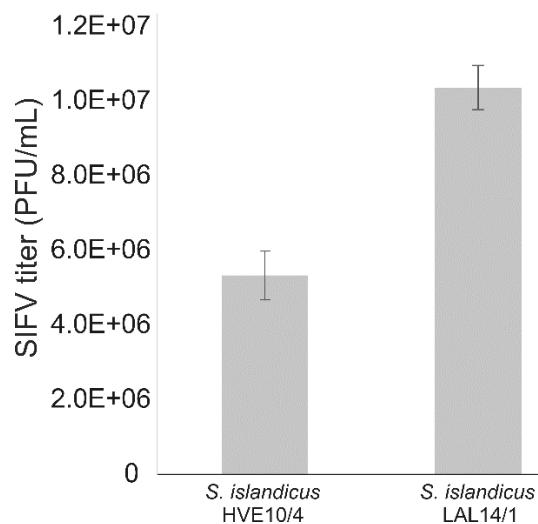


**Figure S10. Comparison of the viral titer obtained upon the infection of two closely related *S. islandicus* strains HVE10/4 and LAL14/1 with SIFV.** After infection of both strains using the same conditions, the viral titer (PFU/mL) was determined by plaque assay, as described in Materials and Methods.

#### SI Video

**Supplementary Video S1.** Bundles of enveloped and non-enveloped virus-like particles in the SIFV-infected cell. The video of a tomogram and rendering corresponds to that in Figure 2F.

## SI Table

**Table S1.** Proteins detected in the five bands (B1-B5) present in the membrane fraction of infected cells and analyzed by LC-MS/MS. Peptide masses were searched against the annotated SIFV proteome.

Band	Gene	Function	Molecular weight (kDa)	Total peptides detected	Sequence coverage (%)	Sum of IBAQ	Protein ID
B1	SIFV0036	Major capsid protein 2	22.5	18	82.8	6.41E+08	Y036_SIFVH
B2	SIFV0035	Major capsid protein 1	18.8	23	82.6	4.33E+08	Y035_SIFVH
B4	SIFV0015	Hypothetical protein	11.7	12	80.8	1.32E+08	Y015_SIFVH
	SIFV0043	Hypothetical protein	10.4	6	31.5	6.80E+07	Y043_SIFVH
	SIFV0020	Hypothetical protein	10.8	9	58.9	5.31E+07	Y020_SIFVH
B5	SIFV0071	Hypothetical protein	8.5	3	39.7	6.09E+06	Y071_SIFVH

## SI References

1. Arnold HP, *et al.* (2000) A novel lipothrixvirus, SIFV, of the extremely thermophilic crenarchaeon *Sulfolobus*. *Virology* 267(2):252-66.
2. Zillig W, *et al.* (1998) Genetic elements in the extremely thermophilic archaeon *Sulfolobus*. *Extremophiles* 2(3):131-40.
3. Jaubert C, *et al.* (2013) Genomics and genetics of *Sulfolobus islandicus* LAL14/1, a model hyperthermophilic archaeon. *Open Biol* 3(4):130010.
4. Quemis ER, *et al.* (2015) *Sulfolobus* spindle-shaped virus 1 contains glycosylated capsid proteins, a cellular chromatin protein, and host-derived lipids. *J Virol* 89(22):11681-91.
5. Uldahl KB, *et al.* (2016) Life cycle characterization of *Sulfolobus* monocaudavirus 1, an extremophilic spindle-shaped virus with extracellular tail development. *J Virol* 90(12):5693-5699.
6. Bize A, *et al.* (2009) A unique virus release mechanism in the Archaea. *Proc Natl Acad Sci U S A* 106(27):11306-11.
7. Quax TE, Krupovic M, Lucas S, Forterre P, & Prangishvili D (2010) The *Sulfolobus* rod-shaped virus 2 encodes a prominent structural component of the unique virion release system in Archaea. *Virology* 404(1):1-4.
8. Kremer JR, Mastrorade DN, & McIntosh JR (1996) Computer visualization of three-dimensional image data using IMOD. *J Struct Biol* 116(1):71-76.
9. Chen M, *et al.* (2017) Convolutional neural networks for automated annotation of cellular cryo-electron tomograms. *Nat Methods* 14(10):983-985.
10. Pettersen EF, *et al.* (2004) UCSF Chimera--a visualization system for exploratory research and analysis. *J Comput Chem* 25(13):1605-12.